CORRECTED 25 JANUARY 2024

SCIENCE ADVANCES | RESEARCH ARTICLE

CHEMISTRY

Misoriented high-entropy iridium ruthenium oxide for acidic water splitting

Chun Hu[1]†, Kaihang Yue[2]†, Jiajia Han[3]*, Xiaozhi Liu[4], Lijia Liu[5], Qiunan Liu[6], Qingyu Kong[7,8], Chih-Wen Pao[9], Zhiwei Hu[10], Kazu Suenaga[6], Dong Su[4], Qiaobao Zhang[3], Xianying Wang[2]*, Yuanzhi Tan[1], Xiaoqing Huang[1]*

Designing an efficient catalyst for acidic oxygen evolution reaction (OER) is of critical importance in manipulating proton exchange membrane water electrolyzer (PEMWE) for hydrogen production. Here, we report a fast, nonequilibrium strategy to synthesize quinary high-entropy ruthenium iridium-based oxide (M-RuIrFeCoNiO_2) with abundant grain boundaries (GB), which exhibits a low overpotential of 189 millivolts at 10 milliamperes per square centimeter for OER in 0.5 M H_2SO_4. Microstructural analyses, density functional calculations, and isotope-labeled differential electrochemical mass spectroscopy measurements collectively reveal that the integration of foreign metal elements and GB is responsible for the enhancement of activity and stability of RuO_2 toward OER. A PEMWE using M-RuIrFeCoNiO_2 catalyst can steadily operate at a large current density of 1 ampere per square centimeter for over 500 hours. This work demonstrates a pathway to design high-performance OER electrocatalysts by integrating the advantages of various components and GB, which breaks the limits of thermodynamic solubility for different metal elements.

INTRODUCTION

Developing a hydrogen economy provides one of the most promising pathways to achieve the goal of decarbonization. Electrocatalytic water splitting has been regarded as an ideal strategy for transforming electricity from intermittent solar and wind sources to produce hydrogen fuel (*1*–*4*). The traditional alkaline liquid electrolysis and the membrane-based, including anion exchange membrane and proton exchange membrane (PEM), water electrolysis are the two mainstream technologies for hydrogen generation. Because of the superiorities of high-purity hydrogen production, large working current density, and fast response time, the PEM water electrolyzer (PEMWE) is receiving more and more research attention. However, the strongly acidic environment under PEMWE working conditions extremely requires the use of noble metals (*5*). In comparison with the cathode hydrogen evolution reaction, which merely involves a two-proton–coupled electron transfer process, the anodic oxygen evolution reaction (OER) experiences a four-electron transfer pathway with sluggish reaction kinetics (*6*, *7*). The ruthenium oxide (RuO_2) has been considered a promising candidate owing to its relatively lower-cost and higher-catalytic activity (*3*, *8*–*10*). However, the unwilling Ru dissolution under OER acidic conditions and inadequate activity call for the development of high-performance RuO_2 electrocatalysts (*11*–*13*).

To date, various approaches have been exploited to enhance the OER performance of RuO_2 such as strain engineering (e.g., the compressive or tensile strain existing on the skin) (*14*, *15*), surface/interface engineering (*16*, *17*), and elemental doping (*18*, *19*). Previous studies have revealed that the incorporation of corrosion-resistance elements could stabilize RuO_2, thus alleviating the generation of soluble high-valence Ru species (*20*). However, the improved stability is usually at the sacrifice of activity. Besides, doping with transition metals has been considered to be an effective approach to improving the activity via modifying the local electronic structure (e.g., d-band center), increasing the concentration of surface active species (e.g., the hydroxyl group), and so on (*21*–*23*), while many transition metals are prone to leaching under acidic OER environment, resulting in the instability of catalysts. Consequently, achieving enhanced activity and considerable stability simultaneously within the RuO_2 counterpart has been formidably challenging.

Here, we select a fast, nonequilibrium method to prepare the grain boundary (GB)–abundant quinary high-entropy oxide, involving five cations (atomic ratio of each cation: 5 to 35%) in a homogeneous phase, via simultaneously introducing acid resistance constituent (Ir) and activity enhancing components (iron, cobalt, and nickel) into RuO_2 lattice (M-RuIrFeCoNiO_2). The design strategy of multicomponent catalyst is there to address the pre-existent issues of inferior stability and limited catalytic activity of RuO_2 under acidic OER conditions. Moreover, the introduction of non-precious transition metal, if it works for the catalytic performance, can reduce the usage of noble metals. The M-RuIrFeCoNiO_2 delivers a high turnover frequency (TOF) value of 0.24 O_2 s^{-1} (at η_{300}), surpassing commercial RuO_2 (0.02 O_2 s^{-1}). Operando differential electrochemical mass spectroscopy (DEMS) reveals that the reaction pathway of oxygen evolution was tuned after incorporating foreign

[1]State Key Laboratory of Physical Chemistry of Solid Surfaces, College of Chemistry and Chemical Engineering, Xiamen University, Xiamen 361005, China. [2]CAS Key Laboratory of Materials for Energy Conversion, Shanghai Institute of Ceramics, Chinese Academy of Sciences, Shanghai 200050, China. [3]Department of Materials Science and Engineering, College of Materials, Xiamen University, Xiamen 361005, China. [4]Beijing National Laboratory for Condensed Matter Physics, Institute of Physics, Chinese Academy of Sciences, Beijing 100190, China. [5]Department of Chemistry, Western University, 1151 Richmond Street, London, ON N6A 5B7, Canada. [6]The Institute of Scientific and Industrial Research, Osaka University, Ibaraki, Osaka 567-0047, Japan. [7]Synchrotron Soleil, L'Orme des Merisiers, St-Aubin, 91192 Gif-sur-Yvette CEDEX, France. [8]School of Physical Science and Information Technology, Liaocheng University, Liaocheng 252059, China. [9]National Synchrotron Radiation Research Center, 101 Hsin-Ann Road, Hsinchu 30076, Taiwan. [10]Max Planck Institute for Chemical Physics of Solids, Nothnitzer Strasse 40, Dresden 01187, Germany.
*Corresponding author. Email: jiajiahan@xmu.edu.cn (J.H.); wangxianying@mail.sic.ac.cn (X.W.); hxq006@xmu.edu.cn (X.H.)
†These authors contributed equally to this work.

atoms. Moreover, density functional theory (DFT) simulations indicate that the integration of the multielement mixing effect and GB synergistically improves the OER activity and stabilizes the catalytic unit. The PEM electrolyzer was assembled by using M-RuIrFeCoNiO_2 and commercial Pt/C as anodic and cathodic catalysts, respectively, which exhibits outstanding long-term durability for operating over 500 hours at an ultrahigh current density of 1 A cm^{-2}, further demonstrating its great potential in the application of water splitting industry.

RESULTS

Synthesis and structural characterization

We synthesized the M-RuIrFeCoNiO_2 catalyst using a nonequilibrium salt melt synthesis method (see details in Materials and Methods). We introduced chemically active 3d transition metals, including iron (Fe), cobalt (Co), and nickel (Ni), and 5d metal iridium (Ir) into the RuO_2 for the sake of enhanced activity and stability, respectively. A homogeneous precursor containing several metal chlorides was rapidly added into the sodium nitrate ($NaNO_3$) ionic melt (350°C), followed by the fast cooling with water to yield GB-abundant nanosheets composed of numerous small nanoparticles (NPs) (Fig. 1A). Here, $NaNO_3$ behaves as solvent and reaction media, in analog to oxobase, which can serve oxide ion O^{2-} and therefore reacts with metal cations to precipitate oxide (*24*). As a Lux-Flood base with relatively strong basicity, the presence of $NaNO_3$ can also accelerate the reaction kinetics (*25*). In contrast to traditional slow cooling, nonequilibrium rapid quenching favors the formation of structural misorientation attachment, such as the GB resulting from the interplay of free energies and reaction dynamics (*26*). More importantly, it was found that the introduction of GB can enhance the activity of catalysts (*27*). For comparison, the M-RuO_2 catalyst was prepared following the same procedure except that ruthenium chloride is the sole metal precursor.

X-ray diffraction (XRD) pattern of M-RuIrFeCoNiO_2 matches the standard rutile RuO_2 phase (JCPDS no. 43-1027) (Fig. 1B) and is similar to that of M-RuO_2 (fig. S1). Atomic force microscopy (AFM) image (Fig. 1C) and dark-field transmission electron microscopy (TEM) image (fig. S2A) reveal that the lateral size of M-RuIrFeCoNiO_2 ranges from the hundreds of nanometers to the micrometer scale. AFM displays that the thickness of M-RuIrFeCoNiO_2 is about several nanometers. Aberration-corrected high-resolution TEM (HRTEM) image shows that M-RuIrFeCoNiO_2 is cobbled together from various NPs, comprising a large population of GB (Fig. 1D). The average size of these NPs is around several nanometers, being consistent with the height of M-RuIrFeCoNiO_2 from AFM measurement. Fast Fourier transform images acquired from Fig. 1D indicate that these NPs presents different crystallographic planes and orientations. The small NPs enable the large exposure of Ru active sites and more effective usage of Ru atoms. The vigorous reaction between precursors and $NaNO_3$ molten salt results in a large amount of nucleation of metal oxide. Subsequently, the formation of kinetically stabilized superstructures of mesocrystals intermediates from these dispersed nucleation centers spontaneously amalgamate by sharing a certain crystallographic orientation at a planar interface. The imperfect oriented attachment of multiple nanocrystals and the ultrafast cooling led to the generation of dislocations with edges (such as GB) to match the orientations of different crystallographic facets and reduce the surface free energy (*28*, *29*). The enlarged HRTEM image clearly shows that these NPs with different orientations are connected by GB. The lattice spacing of 2.58 and 2.21 Å can be assigned to the (101, 200) planes of the rutile RuO_2, respectively (Fig. 1E). Further analyses reveal that these NPs also display the characteristics of single crystal, and the twinning alongside the GB (Fig. 1F). Moreover, the GB can involve one or two atomic layers, accompanying with the mismatch of atomic arrangement by its sides (Fig. 1G). The refined electron energy loss spectroscopy (EELS) spectra extracted from Fig. 1I are shown in Fig. 1H. It is found that Ru M-edge, Ir M-edge, Fe L-edge, Co L-edge, and Ni L-edge as well as O K-edge are simultaneously presented in the NPs. Furthermore, the corresponding elemental mappings reveal that Ru, Ir, Fe, Co, and Ni are homogeneously distributed rather than being phase-segregated (Fig. 1I and fig. S5). To gain more statistics, Ar^+ sputtering–assisted x-ray photoelectron spectroscopy (XPS) was measured on the M-RuIrFeCoNiO_2 (fig. S6). The concentration profiles also show that despite increasing the etching time, Ru, Ir, Fe, Co, and Ni are always present in the sample, indicating that these foreign elements were successfully introduced into the RuO_2. This can be attributed to the ultrafast cooling manipulation that reserves uniform dispersion of multiple elements. Moreover, the configurational entropy of the high-entropy oxide is much larger than that of each single metal oxide, which indicates that this high-entropy oxide is thermodynamically stable at finite temperatures (Supplementary Note). The content of Ru for M-RuIrFeCoNiO_2 is around 28.94 weight % (wt %) as determined by inductively coupled plasma optical emission spectrometry (ICP-OES). Furthermore, as revealed by the Brunauer-Emmett-Teller measurements (fig. S7), M-RuIrFeCoNiO_2 achieves a high specific area of 141.3 $m^2 g^{-1}$, showing the large exposure of catalytic active sites.

Oxidation state and local structure analyses

XPS was used to investigate the surface chemical states of these catalysts. The Ru 3d core level regions of M-RuIrFeCoNiO_2, M-RuO_2, and commercial RuO_2 (C-RuO_2; Perfemiker) show two sets of doublets, showing mixed oxidation states of Ru^{4+} and $Ru^{<4+}$ (*30*). Compared to M-RuO_2 and C-RuO_2, the Ru 3d of M-RuIrFeCoNiO_2 exhibits a negative shift after the incorporation of Ir, Fe, Co, and Ni (Fig. 2A). In addition, Ir 4f XPS result of M-RuIrFeCoNiO_2 exhibits lower binding energy with three sets of peaks, which can be assigned to the Ir^{3+}, Ir^{4+}, and the satellites (fig. S8) (*14*, *27*). The Fe, Co, and Ni 2p XPS spectra in M-RuIrFeCoNiO_2 present the chemical states of oxidative divalent and trivalent (fig. S9) (*31*). With regards to O 1-s spectra, the deconvoluted peaks show negative shifts in binding energies after incorporating foreign elements compared to that of M-RuO_2, which indicates the charge redistribution among these elements (fig. S10) (*18*, *27*, *32*).

Moreover, x-ray absorption near-edge structure (XANES) and extended x-ray absorption fine structure (EXAFS) experiments were performed to elucidate the chemical states and the atomic coordination structures of these catalysts, respectively. Ru-K XANES spectra of M-RuIrFeCoNiO_2 and M-RuO_2 locate at the same energy as that of C-RuO_2 but shift to higher energy relative to that of Ru foil, revealing a Ru^{4+} valence state. The diversity in the leading edge and white shapes of M-RuIrFeCoNiO_2 and M-RuO_2 might be attributed to the differences in the local environment compared to that of C-RuO_2 (Fig. 2B) (*33*, *34*) as found in EXAFS. The Fourier

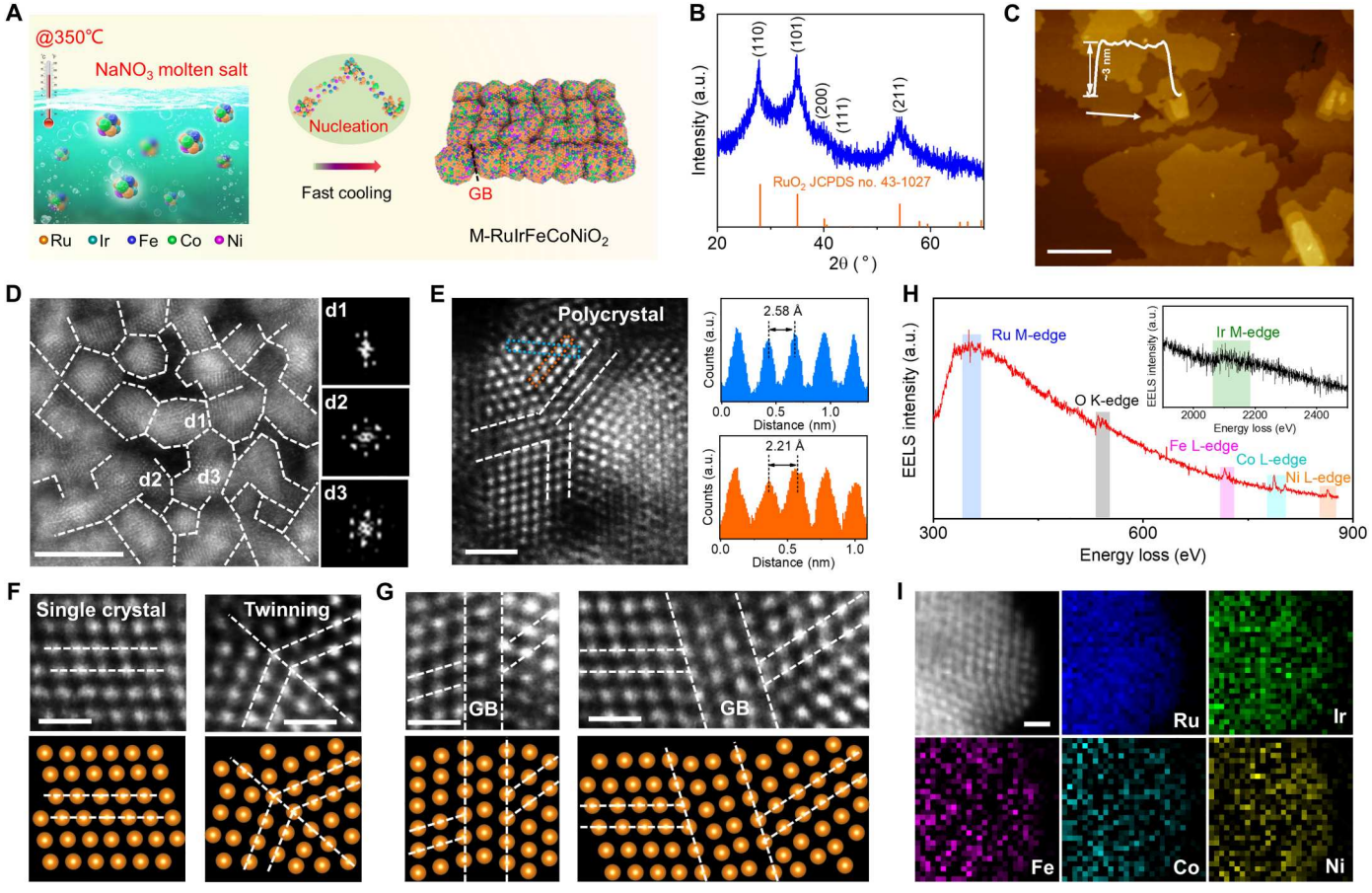

Fig. 1. Synthesis and characterization of high-entropy M-RuIrFeCoNiO$_2$. (**A**) Schematic illustration of the fast, nonequilibrium synthetic process for synthesizing M-RuIrFeCoNiO$_2$, showing the generation of GB. (**B**) X-ray diffraction pattern of M-RuIrFeCoNiO$_2$. (**C**) Atomic force microscopy image of M-RuIrFeCoNiO$_2$. Scale bar, 2 μm. Inset, the thickness of the representative nanosheet. (**D**) Aberration-corrected high-angle annular dark-field scanning transmission electron microscopy (HAADF-STEM) image of M-RuIrFeCoNiO$_2$, with abundant GB marked with white dashed lines (left). The fast Fourier transform patterns indicate the different orientations of nanoparticles (right). Scale bar, 5 nm. (**E**) Magnified HAADF-STEM image of M-RuIrFeCoNiO$_2$, presenting the characteristics of polycrystalline. The white dashed lines highlight the GB. Insets to the right show the corresponding intensity profiles labeled with blue and orange dashed boxes. Scale bar, 1 nm. (**F**) Lattice-resolved HAADF-STEM images of M-RuIrFeCoNiO$_2$ show the presence of a single crystal (top left) and twinning (top right) of nanoparticles. Scale bars, 0.5 nm. (**G**) Lattice-resolved HAADF-STEM images of M-RuIrFeCoNiO$_2$, with different types of GB (top). Scale bars, 0.5 nm. The bottom images in (F) and (G) illustrate the atomic arrangement. The orange spheres and white dashed lines in (F) and (G) denote metal atoms and atomic arrangement directions of M-RuIrFeCoNiO$_2$, respectively. (**H**) Electron energy loss spectroscopy (EELS) spectra of the M-RuIrFeCoNiO$_2$ in (I). (**I**) HAADF-STEM image and elemental mappings of the M-RuIrFeCoNiO$_2$. Scale bar, 0.5 nm. a.u., arbitrary units.

transform EXAFS (FT-EXAFS) spectrum (non-phase shift corrected) of M-RuIrFeCoNiO$_2$ shows a main peak, which is fitted by a Ru-O shell with a bond distance of 1.993 Å, slightly longer than the 1.976 Å distance in M-RuO$_2$, indicating a distorted structure resulting from the incorporation of foreign atoms (table S2). Meanwhile, the coordination number (CN) of M-RuIrFeCoNiO$_2$ is found to be 4.5, which is lower than the value of 6 for standard RuO$_2$. The decrease of the CN value is possibly ascribed to the following factors: a large population of surface and corner atoms in the NPs arising from the decrease in particle size and oxygen vacancies normally presented in oxides. Moreover, the CN is much higher than that of M-RuO$_2$ (3.6). Considering that M-RuIrFeCoNiO$_2$ has a similar particle size to that of M-RuO$_2$, the increase of CN value mainly derives from the partial elimination of oxygen vacancies after incorporating these foreign atoms, as revealed by the electron paramagnetic resonance (EPR) spectra (fig. S12). Appropriate amounts of oxygen vacancies could improve the electronic conductivity of the as-prepared materials (*35*, *36*). Nevertheless, the lack of contributions of distant coordination shells suggests a much more disordered structure in M-RuIrFeCoNiO$_2$ than in the well-defined crystalline RuO$_2$ materials (Fig. 2C, figs. S13 to S15, and table S2). At the Ir L$_3$-edge, the white line position of M-RuIrFeCoNiO$_2$ is close to IrO$_2$ (Fig. 2D), indicating an Ir^{4+} valence state. The corresponding EXAFS fitting reveals that the CN of the first coordination shell (Ir-O) is 5.2, slightly lower than the predicted value of 6. The Ir-O bond length in M-RuIrFeCoNiO$_2$ is around 1.995 Å (figs. S16 to S18 and table S3), which is slightly smaller than the value of standard IrO$_2$ (2.021 Å). The O K-edge absorption spectra of M-RuIrFeCoNiO$_2$ and M-RuO$_2$ resemble closely with four main features labeled (A, B, C, and D) (Fig. 2E). The two pre-edge peaks denoted by A and B in M-RuO$_2$ can be assigned to t_{2g} and e_g orbitals hybridized with unoccupied O 2p states (*22*, *37*). In the pre-edge region of the O-K x-ray absorption spectroscopy (XAS) spectrum of M-RuIrFeCoNiO$_2$, peaks A and B can

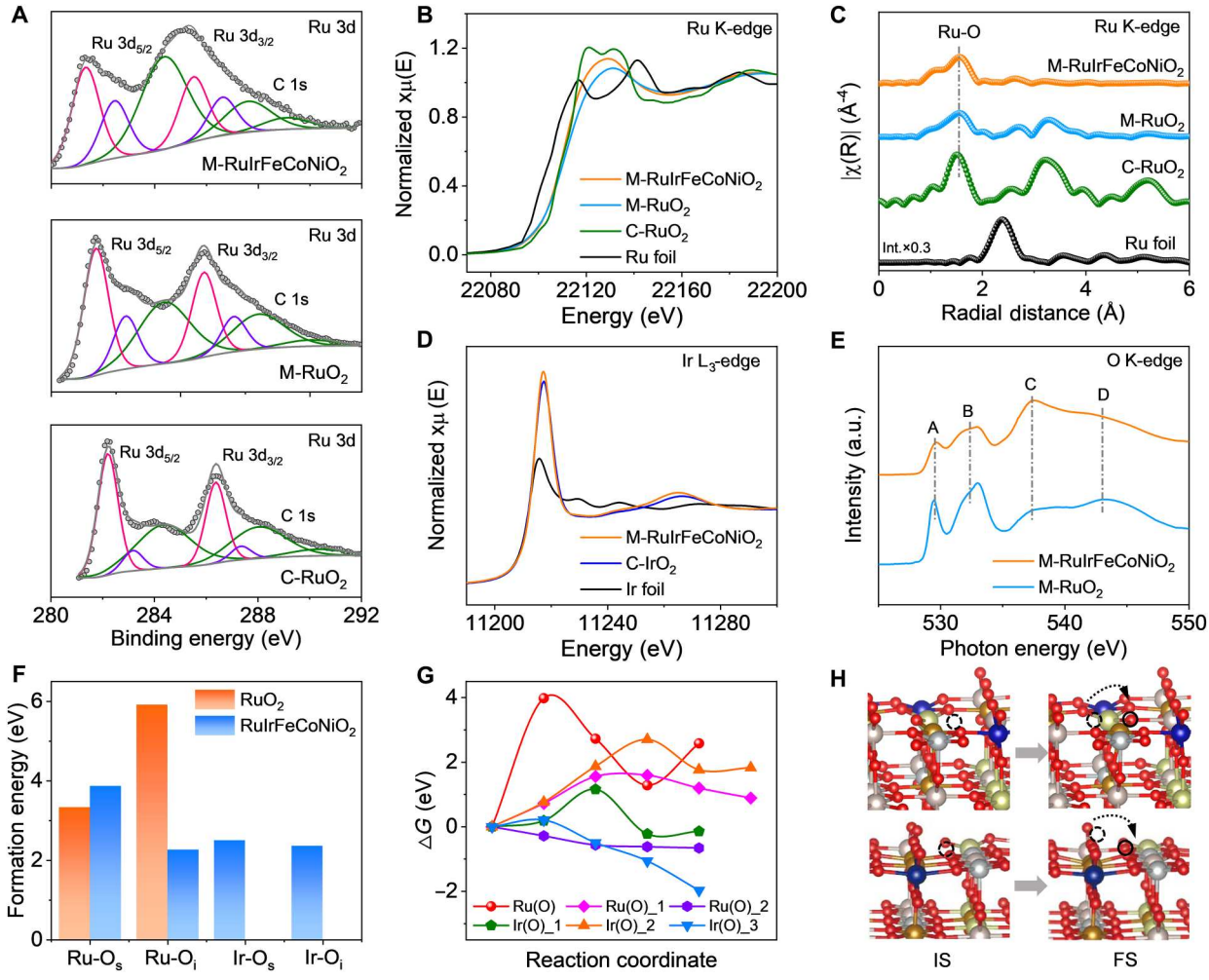

Fig. 2. Chemical state and coordination environment. (**A**) Ru 3d XPS spectra of M-RuIrFeCoNiO$_2$, M-RuO$_2$, and C-RuO$_2$. (**B**) Ru K-edge x-ray absorption near-edge structure (XANES) spectra of M-RuIrFeCoNiO$_2$, M-RuO$_2$, C-RuO$_2$, and Ru foil. (**C**) Fourier transformed x-ray absorption fine structure k^3-weighted χ(R) function spectra of Ru M-RuIrFeCoNiO$_2$, M-RuO$_2$, C-RuO$_2$, and Ru foil (non-phase shift corrected). (**D**) Ir L$_3$-edge XANES spectra of M-RuIrFeCoNiO$_2$, C-IrO$_2$, and Ir foil. (**E**) O K-edge soft x-ray absorption spectroscopy (XAS) spectra of M-RuIrFeCoNiO$_2$ and M-RuO$_2$. (**F**) Formation energy of O vacancy in RuO$_2$ and RuIrFeCoNiO$_2$. O$_s$ and O$_i$ refer to the surface and inner oxygen that coordinate with Ru/Ir, respectively. The hazel, pale green, tan, cyaneous, gray, and red spheres in the atomic models represent Ru, Ir, Fe, Co, Ni, and O atoms, respectively. (**G**) Free energy diagram for oxygen diffusion of Ru-coordinated oxygen in RuO$_2$ [Ru(O)] and RuIrFeCoNiO$_2$ [Ru(O)_1, and Ru(O)_2], and Ir-coordinated oxygen in RuIrFeCoNiO$_2$ [Ir(O)_1, Ir(O)_2, and Ir(O)_3]. IS and FS represent the initial state and final state, respectively. (**H**) Representative models for IS and FS of Ru(O)_2 (top) and Ir(O)_3 (bottom) in (G).

be still seen, but the relative spectral weight is decreased due to incorporating more 3d transition elements, which have weak covalence with O 2p. Moreover, the broader features at high energy levels labeled as C and D are due to excitations into O 2p states hybridized with M-sp states (*22*, *37*–*40*).

It is widely accepted that the states of O atoms in catalysts are very important since they closely relate to the structural stability during the target OER. To confirm our experimental results and investigate the stability of the aim catalyst, we calculated the formation energy and diffusion barrier of Ru/Ir-coordinated O atom based on DFT, and here, the Ru in RuO$_2$ and RuIrFeCoNiO$_2$ and Ir in RuIrFeCoNiO$_2$ were selected for comparison. The results show that the vacancy formation energy of Ru coordination O atoms in RuIrFeCoNiO$_2$ is higher than that of Ru coordination O atoms in RuO$_2$ (Fig. 2F). Although the vacancy formation energy of Ir coordination O atoms in RuIrFeCoNiO$_2$ (Fig. 2F) is lower than that of Ru coordination O atoms in RuO$_2$, the diffusion barrier of the former is much lower, and even the Ir can grab the coordination O of the surrounding Fe/Co/Ni metal atoms. A similar phenomenon is also found in Ru coordination O atoms in RuIrFeCoNiO$_2$ (Fig. 2, G and H, and fig. S19). That is, the defects formed by the coordination O vacancies of Ru/Ir atoms can be much more readily repaired by the diffusion of the nearest and second nearest neighbor Fe/Co/Ni coordination O atoms to maintain structural stability. In addition, the energy change required to lose surface oxygen is 3.33 and 3.87 eV for RuO$_2$ and RuIrFeCoNiO$_2$, respectively, indicating that the surface oxygen becomes more stable during the OER process when introducing Ir, Fe, Co, and Ni foreign atoms (fig. S20) (*41*).

Electrocatalytic OER performance

The OER performance of various catalysts was evaluated in 0.5 M H_2SO_4 by linear sweep voltammetry (LSV). The C-RuO_2 and commercial Ir/C (C-Ir/C; CAS Cotrun New Energy, 20 wt %) were used as references. As depicted in Fig. 3A, M-RuIrFeCoNiO_2 merely requires an overpotential of 189 mV to deliver the current density of 10 mA cm^{-2} (η_{10}), which outperforms M-RuO_2 (210 mV), C-RuO_2 (253 mV), and C-Ir/C (292 mV). The M-RuIrFeCoNiO_2 also shows a lower overpotential of 233 (η_{50}) and 262 mV (η_{100}) in comparison with other references (fig. S21). The corresponding Tafel curves further exhibit that M-RuIrFeCoNiO_2 has a lower slope of 49 mV $decade^{-1}$, compared to the values of other control samples (fig. S22), showing a fast kinetic charge transfer within M-RuIrFeCoNiO_2 (*42*). As revealed by electrochemical impedance spectroscopy (EIS), M-RuIrFeCoNiO_2 shows the smallest charge transfer resistance (R_{ct}) among these samples, demonstrating the fastest oxygen evolution kinetics on the M-RuIrFeCoNiO_2 (fig. S23).

Moreover, M-RuIrFeCoNiO_2 achieves a specific activity of 1.17 mA cm^{-2}_{ECSA} at η_{300} which exceeds the M-RuO_2 (0.66 mA cm^{-2}_{ECSA}), C-RuO_2 (0.27 mA cm^{-2}_{ECSA}), and C-Ir/C (0.09 mA cm^{-2}_{ECSA}) (Fig. 3B). To further evaluate the intrinsic activity of the catalysts, the TOF was calculated (details in Materials and Methods). Obviously, M-RuIrFeCoNiO_2 gives rise to the highest TOF values of 0.24 O_2 s^{-1} (normalized to all Ru + Ir atoms) at

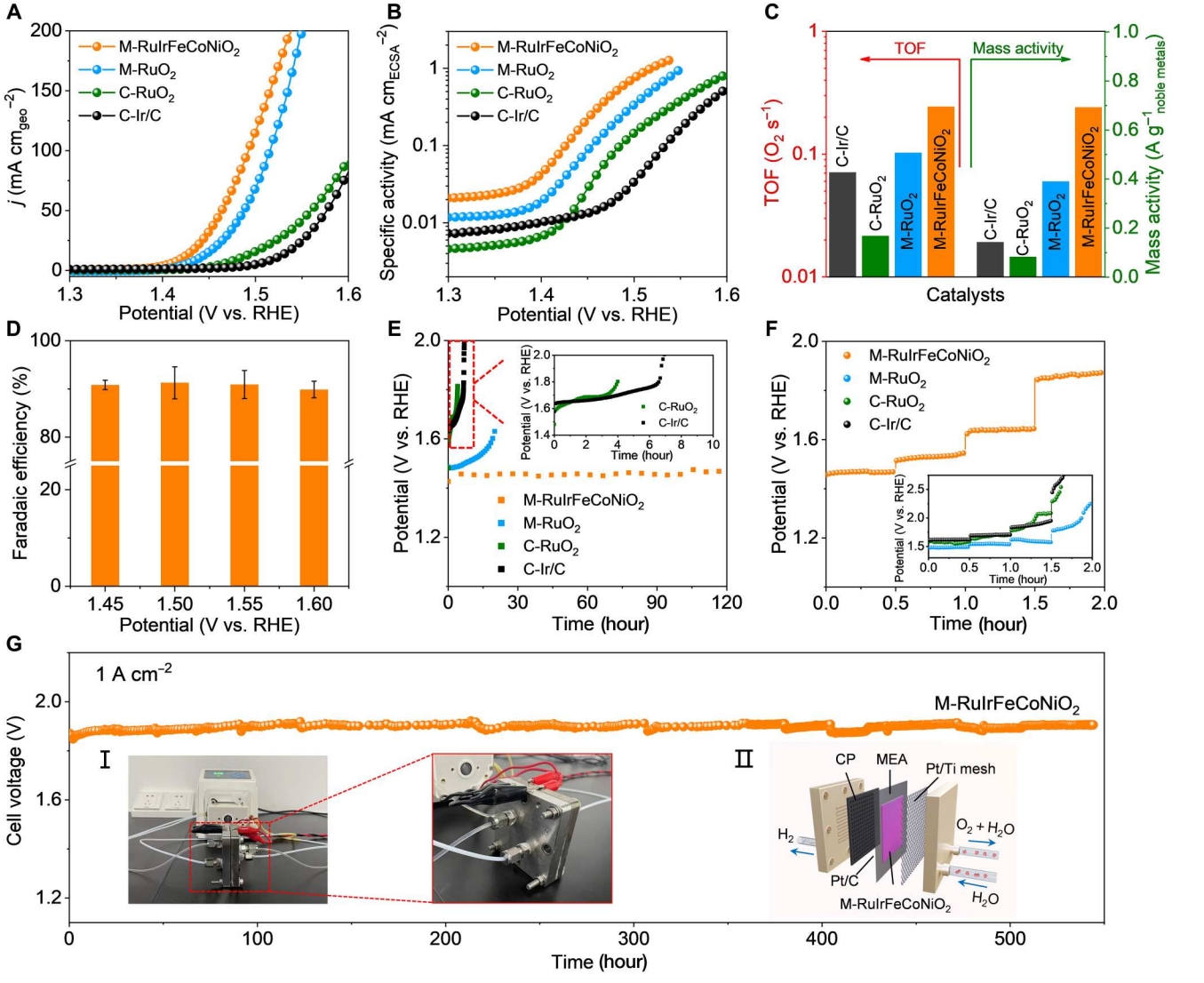

Fig. 3. Electrocatalytic OER properties of various catalysts in 0.5 M H_2SO_4. (**A**) Polarization curves of M-RuIrFeCoNiO_2, M-RuO_2, and commercial control catalysts (C-RuO_2 and C-Ir/C) with iR correction. (**B**) Specific activity [normalized by electrochemically active surface area (ECSA)] of M-RuIrFeCoNiO_2, M-RuO_2, C-RuO_2, and C-Ir/C. (**C**) Comparison of TOF and mass activities of M-RuIrFeCoNiO_2, M-RuO_2, C-RuO_2, and C-Ir/C at an overpotential of 300 mV. (**D**) Faradaic efficiency of M-RuIrFeCoNiO_2 at applied different potentials. (**E**) Chronopotentiometric curves of M-RuIrFeCoNiO_2, M-RuO_2, C-RuO_2, and C-Ir/C at 10 mA cm^{-2} in 0.5 M H_2SO_4. (**F**) Chronopotentiometry durability test with different applied current densities (at 50, 100, 200, 500 mA cm^{-2}, respectively) for M-RuIrFeCoNiO_2, M-RuO_2, C-RuO_2, and C-Ir/C. (**G**) Chronopotentiometric response of M-RuIrFeCoNiO_2 at 1 A cm^{-2} in the PEM electrolyzer [Inset: (I) photograph of the PEM electrolyzer device and (II) schematic illustration of the PEM electrolyzer].

η_{300} (Fig. 3C, left), which is 2.4, 3.5, and 12.1 times higher than that of M-RuO_2, C-Ir/C, and C-RuO_2, respectively. The TOF value of M-RuIrFeCoNiO_2 is also superior to other catalysts (table S4). The real TOF value should be much higher than the theoretical value since the calculations assumed all the Ru and/or Ir atoms were active sites in the OER process. With respect to the mass activity (MA), M-RuIrFeCoNiO_2 achieves MA value of 691 A g_{Ru+Ir}^{-1} at η_{300}, which is 1.8 times higher than that of M-RuO_2 (389 A g_{Ru}^{-1}), 4.9 times higher than C-Ir/C (141 A g_{Ru}^{-1}), and 8.5 times higher C-RuO_2 (81 A g_{Ru}^{-1}) (Fig. 3C, right). Besides that, the generated O_2 during the OER process was detected by gas chromatography. The Faradaic efficiency (FE) of M-RuIrFeCoNiO_2 is more than 90% under a wide range of potentials (Fig. 3D and fig. S26). We compared the OER activity of M-RuIrFeCoNiO_2 with the previously published works in terms of η_{10}, Tafel slope, and noble metal loading, where M-RuIrFeCoNiO_2 performed better than most of the reported Ru/Ir-based OER electrocatalysts, validating its outstanding activity (table S5).

The stability of catalysts in acidic media is another key criterion for OER performance. The accelerated durability test with voltammetric cycling in the OER potential window of M-RuIrFeCoNiO_2 reveals a negligible degradation after 1000 cycles (fig. S27A), which is superior to that of M-$RuIrO_2$ (fig. S28A), and comparable to M-IrO_2 (fig. S28B). In contrast, an obvious decay is observed in M-RuO_2 and C-RuO_2. In particular, M-RuO_2 shows less decay in comparison with C-RuO_2, indicating that the GB can improve the stability of the catalyst (fig. S27, B and C). Moreover, the incorporation of Ir can further stabilize the RuO_2. Figure 3E shows the chronopotentiometric responses of M-RuIrFeCoNiO_2, M-RuO_2, C-RuO_2, and C-Ir/C in a three-electrode cell. The η_{10} of M-RuIrFeCoNiO_2 displays a slow overpotential ascending of 0.3 mV $hour^{-1}$ during the whole operating period of 120 hours. Note that the detachment of the catalyst from the support is a factor that would affect the catalyst stability, of which the continuous production of bubble exfoliates the catalyst from the electrode. In contrast, other control samples exhibit a rapid degradation in the early stage. The cations dissolved are inevitable during the OER test in acidic media, especially Fe, Co, and Ni metal ions. The time-dependent cation concentration in the electrolyte during the chronopotentiometry test (at 50 mA cm_{geo}^{-1}) was detected using inductively coupled plasma mass spectroscopy (ICP-MS). As shown, the Fe, Co, and Ni cations leached out of the M-RuIrFeCoNiO_2 rapidly in the first 2 hours, and then slowed down for the next hours (66, 62, and 66 wt % of cations remained for Fe, Co, and Ni, respectively). Ru and Ir ions encountered dissolution at the beginning of the reaction and maintained nearly unchanged thereafter (cations reserved after 10 hours: 84 wt % of Ru and 90 wt % of Ir) (fig. S29 and table S6). The higher dissolution in the initial stage can be assigned to the dissolution of lattice defects and unstable sites, and then the palliative situation indicates the stabilization of the catalyst. To elucidate the stability enhancement of the RuO_2 framework in M-RuIrFeCoNiO_2 after the introduction of Ir, we calculated the stability number (S-number) of M-RuIrFeCoNiO_2 and M-RuO_2. As shown in fig. S30, M-RuIrFeCoNiO_2 shows a markedly high S-number of 5.7×10^4, which is 13.2 times higher than that of M-RuO_2 (0.43×10^4). The multicurrent analyses (using different applied current densities ranging from 50 to 500 mA cm^{-2}) further indicate the enhanced durability of M-RuIrFeCoNiO_2, especially under the large current density (e.g., 500 mA cm^{-2}), in comparison with M-RuO_2, C-RuO_2, and C-Ir/C (Fig. 3F).

In addition, the used catalysts were collected for further characterization. XRD pattern reveals that the RuO_2 phase in M-RuIrFeCoNiO_2 could be well retained after the stability test (fig. S31). The HRTEM image and energy-dispersive x-ray spectroscopy (EDS) mapping suggest that the NPs with abundant GB for M-RuIrFeCoNiO_2 still exist, together with the uniform distributions of Ru, Ir, Fe, Co, and Ni species, despite of a few decreased intensities of Fe, Co, and Ni elements (fig. S32). In addition, Ir 4f XPS signal shows a complete tetravalent form in M-RuIrFeCoNiO_2 after the durability test (fig. S33). On the other hand, Ru 3p XPS spectra depict the varying degrees of increased valence states of Ru in M-RuIrFeCoNiO_2, M-RuO_2, and C-RuO_2 compared with the pristine ones. Moreover, note that M-RuIrFeCoNiO_2 is prone to remain in the lowest chemical state among these catalysts after the accelerated durability test (fig. S34).

Subsequently, we applied the as-prepared M-RuIrFeCoNiO_2 in a PEM electrolyzer (anode) at 80°C, and the commercial Pt/C served as the cathodic catalyst. When applying a large current density of 1 A cm^{-2}, the cell voltage can be maintained over 500 hours of electrolysis with tiny decay, implying the potential of practical application for M-RuIrFeCoNiO_2 catalyst (Fig. 3G). DFT calculations show that when Ir, Fe, Co, and Ni are introduced into the RuO_2, the energy change of Ru demetallization increases from 3.95 to 5.06 eV, implying that RuIrFeCoNiO_2 has a more stable surface Ru than RuO_2 (fig. S37). Moreover, it is also found that the incorporation of Ir, Fe, Co, and Ni can effectively stabilize the lattice oxygen during the OER process (Fig. 2, F and G, and fig. S20) (*41*).

Insights into the catalytic mechanism

To investigate the influence of foreign metal ions and GB on catalyst and reaction intermediates when operating at OER conditions, operando Raman measurements were conducted on the homemade Teflon electrochemical cell equipped with a confocal microscope Raman system (fig. S38A). The operating potentials were chosen ranging from near the initial open circuit potential of the sample to an anodic potential limit of 1.6 V versus Reversible Hydrogen Electrode (RHE). On the basis of Raman-active phonon frequencies calculated by group theory, the rutile RuO_2 phase has the vibration bands of E_g (528 cm^{-1}), A_{1g} (646 cm^{-1}), and B_{2g} (716 cm^{-1}) (*43*). As shown in fig. S38 (B and C), E_g, A_{1g}, and B_{2g} vibration modes are clearly observed in C-RuO_2, while the B_{2g} phonon band is not well resolved in the Raman spectroscopy of M-RuIrFeCoNiO_2. Moreover, the peak at 480 cm^{-1} is also assigned to the additional vibration mode of RuO_2. The E_g mode in M-RuIrFeCoNiO_2 appears the features of blue shift and broadening compared to that in C-RuO_2, which might be due to the difference of particle size and/or the incorporation of foreign elements (*44*, *45*). A blue shift and a spread of E_g peak in M-RuIrFeCoNiO_2 emerge when the anodic potentials continuously lift, which may derive from the appearance of an active state and the reduction of symmetry, respectively, during the OER process (*46*). With the increase of anodic potential, a peak at around 600 cm^{-1} disappears. This could be attributed to the extraction of electrons from $Ru^{<4+}$, representing the oxidative process on these two catalysts, which is in accordance with the XPS analysis (*46*). For M-RuIrFeCoNiO_2, during the positive-going potential excursion, the peak located at 380 to 440 cm^{-1} and ~620 cm^{-1} emerges, which corresponds to hydrous RuO_2

and IrO_2, respectively (*46*, *47*). The presence of GB and the "Cocktail" effect arising from inter-elemental reactions and lattice distortion contribute to the generation of highly active states under anodic potentials, of which hydrous RuO_2 and IrO_2 species are responsible for the remarkable catalytic activity and stability, respectively (*48*, *49*). For C-RuO_2, there is no abovementioned structural evolvement. This may be attributed to the structural collapse of pure RuO_2, which is peculiarly prone to happen under acidic OER conditions (*50*).

To further elucidate the oxygen evolution mechanism that occurs on the M-RuIrFeCoNiO_2 and M-RuO_2, isotope-labeled operando DEMS measurements were carried out using 0.5 M H_2SO_4 $H_2{}^{18}O$ and $H_2{}^{16}O$ electrolyte (Fig. 4, A to C, and figs. S39 and S40). First, M-RuIrFeCoNiO_2 and M-RuO_2 were loaded on the porous Au film and labeled the catalyst surface with ^{18}O by performing five cycles (1.2 to 1.55 V versus RHE) in the 0.5 M H_2SO_4 $H_2{}^{18}O$ electrolyte. Then, the ^{18}O-labeled catalysts were washed with a large amount of water to remove the adsorbed $H_2{}^{18}O$, followed by three cycling in the 0.5 M H_2SO_4 $H_2{}^{16}O$ electrolyte. The gaseous oxygen products containing $^{32}O_2$ ($^{16}O^{16}O$), $^{34}O_2$ ($^{16}O^{18}O$), and $^{36}O_2$ ($^{18}O^{18}O$) were probed by online mass spectroscopy at each cycle. In this case, the oxygen molecule products are widely considered to be formed by three pathways: (i) from two water molecules ($H_2{}^{16}O$) without lattice oxygen participation ($^{16}O^{16}O$), (ii) the combination of one water molecule ($H_2{}^{16}O$) and one lattice oxygen (^{18}O), and (iii) from two lattice oxygen without participation of water (*51*). As depicted in Fig. 4 (B and C), M-RuIrFeCoNiO_2 produced $^{32}O_2$ and $^{34}O_2$, and the $^{36}O_2$ product was not evolved as reflected by the mass signals, while the $^{36}O_2$ signals were evidently discernible on M-RuO_2. Note that the remaining surface $H_2{}^{18}O$ adsorbates are probably involved in the reaction to produce $^{36}O_2$ species. Although the specific area of M-RuIrFeCoNiO_2 is lower than that of M-RuO_2, the amount of surface adsorbed H_2O for M-RuIrFeCoNiO_2 is higher than M-RuO_2 as shown in O 1-s XPS spectra (fig. S10). Note that the particle size and the GB-enriched morphology are similar for these two catalysts; the influence of

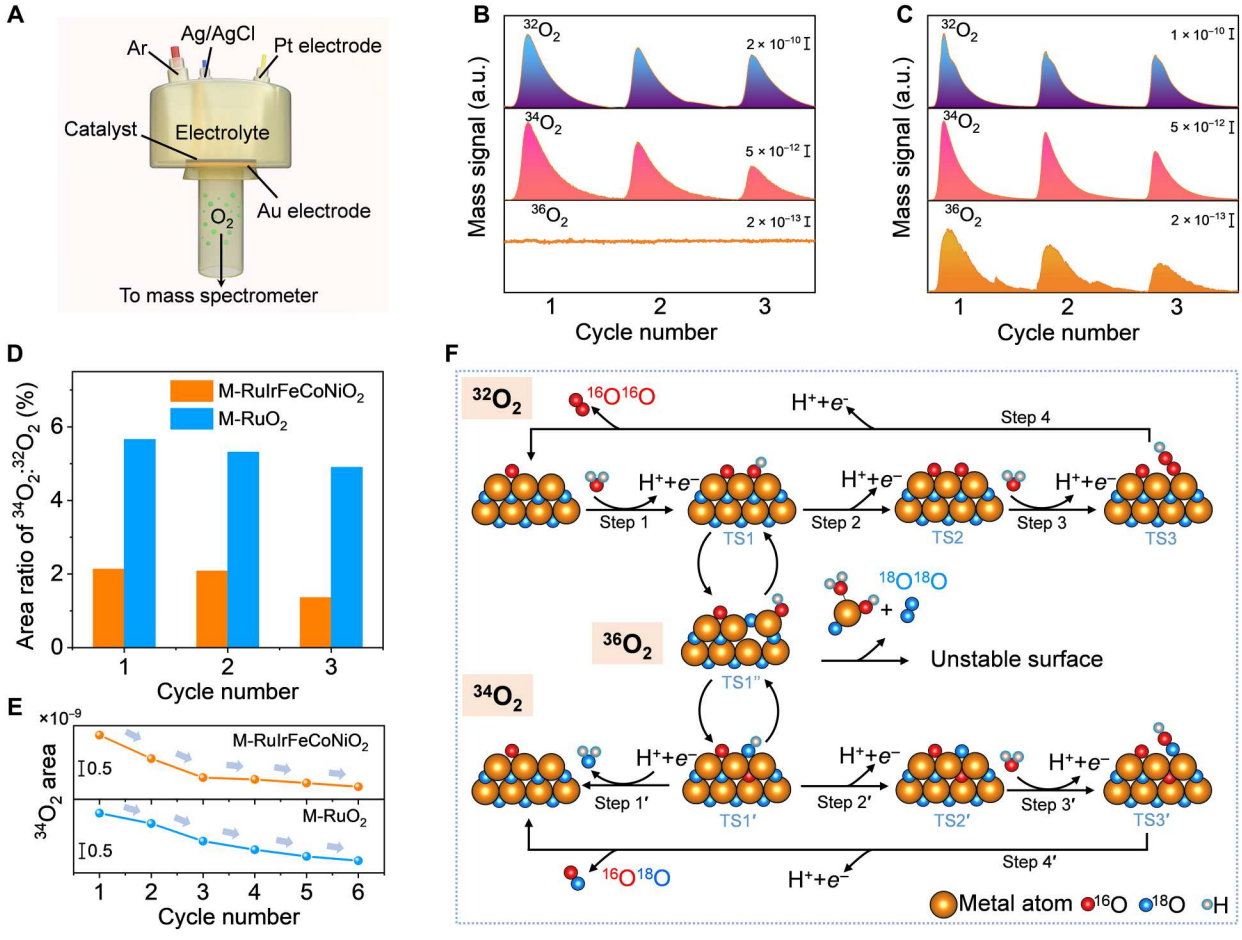

Fig. 4. OER catalytic mechanism analyses. (**A**) Schematic illustration of the operando DEMS. (**B** and **C**) DEMS signals of $^{32}O_2$ [$^{16}O^{16}O$, mass/charge ratio (*m*/*z*) = 32], $^{34}O_2$ ($^{16}O^{18}O$, *m*/*z* = 34), and $^{36}O_2$ ($^{18}O^{18}O$, *m*/*z* = 36) from the gaseous products for ^{18}O-labeled M-RuIrFeCoNiO_2 (B) and M-RuO_2 (C) catalysts in $H_2{}^{18}O$ aqueous H_2SO_4 electrolyte during three times of cycles in the potential range of 1.2 to 1.55 V versus RHE at a scan rate of 10 mV s^{-1}. (**D**) The mass spectroscopy peak area ratio of $^{34}O_2/^{32}O_2$ for M-RuIrFeCoNiO_2 and M-RuO_2. (**E**) Area of $^{34}O_2$ DEMS signals for M-RuIrFeCoNiO_2 and M-RuO_2 during six cycles in the potential range of 1.2–1.55 V versus RHE at a scan rate of 10 mV s^{-1}. (**F**) Proposed OER mechanism for as-prepared M-RuIrFeCoNiO_2 and M-RuO_2, based on the DEMS measurements. The top trajectory represents the dominant adsorbate evolution mechanism (AEM; $^{32}O_2$ signal from DEMS measurements). Both the bottom and middle trajectories denote the lattice oxygen oxidation mechanism ($^{34}O_2$ and $^{36}O_2$ signals from DEMS measurements, respectively). The top and bottom paths involve only one active site, while the middle one follows two active sites. The orange, red, blue, and gray balls denote metal atoms in catalysts, ^{18}O, ^{16}O, and H atoms, respectively (*51*, *52*).

physically absorbed $H_2{}^{18}O$ could be neglected. The ratio of both $^{34}O_2$ and $^{36}O_2$ generated on M-RuIrFeCoNiO$_2$ is much lower than that on M-RuO$_2$, implying the inhibitory effect of lattice oxygen participation (lattice oxygen oxidation mechanism, LOM) on M-RuIrFeCoNiO$_2$ (Fig. 4D). In this approach, though the inevitable dissolution of Fe, Co, and Ni would lead to the active uncoordinated oxygen atoms, which is very likely to participate in the LOM process, the presence of Ir can fasten these oxygen atoms from releasing in the form of oxygen molecules. With the increase of CV cycles, the gradually decreasing $^{34}O_2$ signal indicates the consumption of labeled ^{18}O isotope (Fig. 4E). The suggested reaction pathways are illustrated in Fig. 4F. As hinted by DEMS measurements, both M-RuIrFeCoNiO$_2$ and M-RuO$_2$ follow the main conventional "metal peroxide" pathway [adsorbate evolution mechanism (AEM)] including four concerted proton-electron transfers (top row). Water molecules from the environment encounter a series of deprotonation processes and O-O coupling on metal oxide surface, involving HO*, O*, and HOO* intermediates. In this path, the source of O_2 products ($^{32}O_2$) merely comes from electrolytes ($^{16}O^{16}O$). Another possible pathway results in lattice oxygen evolution (LOM), and this path is identical to that of the AEM process, except that the O_2 molecule ($^{34}O_2$) is composed of one labeled lattice oxygen (^{18}O) and one environmental oxygen (^{16}O) (bottom row). Note that the occurrence of the $^{34}O_2$ process usually implies the beginning of an unstable oxide surface. The oxide surface suffers a destabilized state from TS1 to TS1′ for triggering this reaction pathway. The formation of the destabilized state increases the possibility of oxide dissolution and the participation of more lattice oxygen (^{18}O) to generate $^{36}O_2$ (middle row) (*51*, *52*), as was detected in the M-RuO$_2$ catalyst (Fig. 4C). In addition, previous work reported that the electrophilic *OH intermediates can be probed by methanol electro-oxidation (*53*). Consequently, we investigated the CV curves of M-RuIrFeCoNiO$_2$ before and after the addition of methanol. The clear change of current density after the incorporation of methanol reveals the generation of *OH intermediates through an anodic oxidation process (fig. S41). In summary, the operando Raman spectroscopy dynamically recorded the electrochemical behaviors of M-RuIrFeCoNiO$_2$ and C-RuO$_2$ under the anodic OER process, which shows the formation of robust active Ru/IrO$_x$·xH$_2$O species when applying anodic potentials. Isotope-labeling DEMS measurements precisely probed the real-time gaseous oxygen products from the oxygen evolution procedure in M-RuIrFeCoNiO$_2$ and M-RuO$_2$ catalysts, indicating that the incorporation of Ir can effectively inhibit the participation of lattice oxygen during OER to stabilize the RuO$_2$. The methanol oxidation result suggests the formation of *OH intermediates on the M-RuIrFeCoNiO$_2$ during the OER process.

To further explore the impact of co-doping of transition metals (Ir, Fe, Co, and Ni) and GB formed by different crystallographic orientations on OER activity of RuO$_2$, DFT computations were carried out by establishing RuO$_2$, RuIrO$_2$ [$(Ru_{0.7}Ir_{0.3})O_2$], RuIrFeCoNiO$_2$ [$(Ru_{0.4}Ir_{0.2}Fe_{0.2}Co_{0.1}Ni_{0.1})O_2$], and GB-RuO$_2$ models (fig. S46). The partial density of states in Fig. 5A demonstrates the metal behaviors with high spin states of all these four models. The metallic-like conductor featured by the O 2p and Ru 4d of RuO$_2$ dominating the Fermi level (E_F) is in qualitative agreement with the results from previous computational studies (*54*, *55*). Transition metal doping leads to an increased bonding and fewer antibonding states of O 2p states and metal d states, which is particularly evident in the RuIrFeCoNiO$_2$ model. Under the multielement modulation, Ru atoms transfer electrons to other metal atoms, and the reduced antibonding states enhance the structural stability of the catalyst. The GB formed by RuO$_2$ with different crystallographic orientations similarly increases the occupancy states near the E_F, indicating that the electron migration at the GB is also enhanced. The charge density diagram near the E_F (E_F − 0.1 to E_F) (Fig. 5B) intuitively shows that the electron transfer of RuO$_2$ and RuIrO$_2$ basically depends on metal atoms on the surface of the catalyst. Meanwhile, that of RuIrFeCoNiO$_2$ can come from both the surface and internal atoms, showing excellent electrical conductivity. In addition, GB formed by different crystallographic orientations of RuO$_2$ also has a positive effect on conductivity. The charge density difference (CDD) (Fig. 5C) clearly shows the electrovalent cloud formed by the d state of the metal atoms and the p state of the oxygen atom. Nevertheless, Bader charge analysis quantifies the different numbers of transferred electrons at the active site for these four models, namely, 2.30 e^- for RuIrFeCoNiO$_2$ and 1.97 e^- for GB-RuO$_2$, more than the 1.68 e^- for RuO$_2$ and 1.76 e^- for RuIrO$_2$ (Fig. 5D).

The free energies of the four elementary steps in OER (* + 2H$_2$O → OH* → O* → OOH* → O$_2$) were calculated to uncover the role of transition metals and GB on the electrocatalytic performance (Fig. 5E and fig. S47). The transition metals including the Ru atom with a CN of 5 were considered as the active site (*56*). We noticed that RuO$_2$ and RuIrO$_2$ have a strong adsorption effect on OH^- in the first step, which will inevitably lead to large potentials of subsequent reactions (*57*). The results in Fig. 5E show that the rate-determining step (RDS) in the four-electron process for RuO$_2$ is the formation of O*, with ΔG(O*) − ΔG(OOH*) of 1.84 eV (*58*), while that for RuIrO$_2$ is the formation of O$_2$, and the free energy required from OOH* to O$_2$ is 1.89 eV. After doping transition metals, the adsorption ability of OH^- on the catalyst surface is obviously reduced. Although the final RDS of RuIrFeCoNiO$_2$ is still the formation of O$_2$, the energy required is only 1.56 eV, which is much lower than the 1.89 eV of RuIrO$_2$ and the 1.84 eV of RuO$_2$. The Ru atom on the GB of the RuO$_2$ catalyst also weakens the adsorption of OH^-, resulting in an RDS of the formation of OH* during OER, with ΔG(OH*) of 1.71 eV. Apparently, the introduction of transitional metals and the GB formed by different crystallographic orientations of RuO$_2$ are effective strategies to greatly improve the electrocatalytic performance of RuO$_2$. We then shift the chemical potential of the electrons by the equilibrium potential of U_0 = 1.23 eV, corresponding to the case where the electrode has the thermodynamically allowed maximum potential (*57*). The overpotentials required for the OER for RuO$_2$, RuIrO$_2$, RuIrFeCoNiO$_2$, and GB-RuO$_2$ were determined as 0.61, 0.66, 0.33, and 0.56 eV, respectively. RuIrFeCoNiO$_2$ and GB-RuO$_2$ exhibit excellent electrocatalytic properties compared to RuO$_2$ and RuIrO$_2$. Although the calculated OER overpotential does not directly correspond to the experimental values due to the former being obtained from the thermodynamic analyses (*59*), the reduction in the overpotential by incorporation of transitional metal elements and GB can be confirmed.

We found that the d-band center of RuIrFeCoNiO$_2$ (−1.45) and GB-RuO$_2$ (−1.79) is more negative than that of RuO$_2$ (−1.08), suggesting that the adsorption of intermediates should be weakened during OER (Fig. 5F). Notably, the d-band center of RuIrO$_2$ is the most negative (−1.83) and theoretically should have the lowest

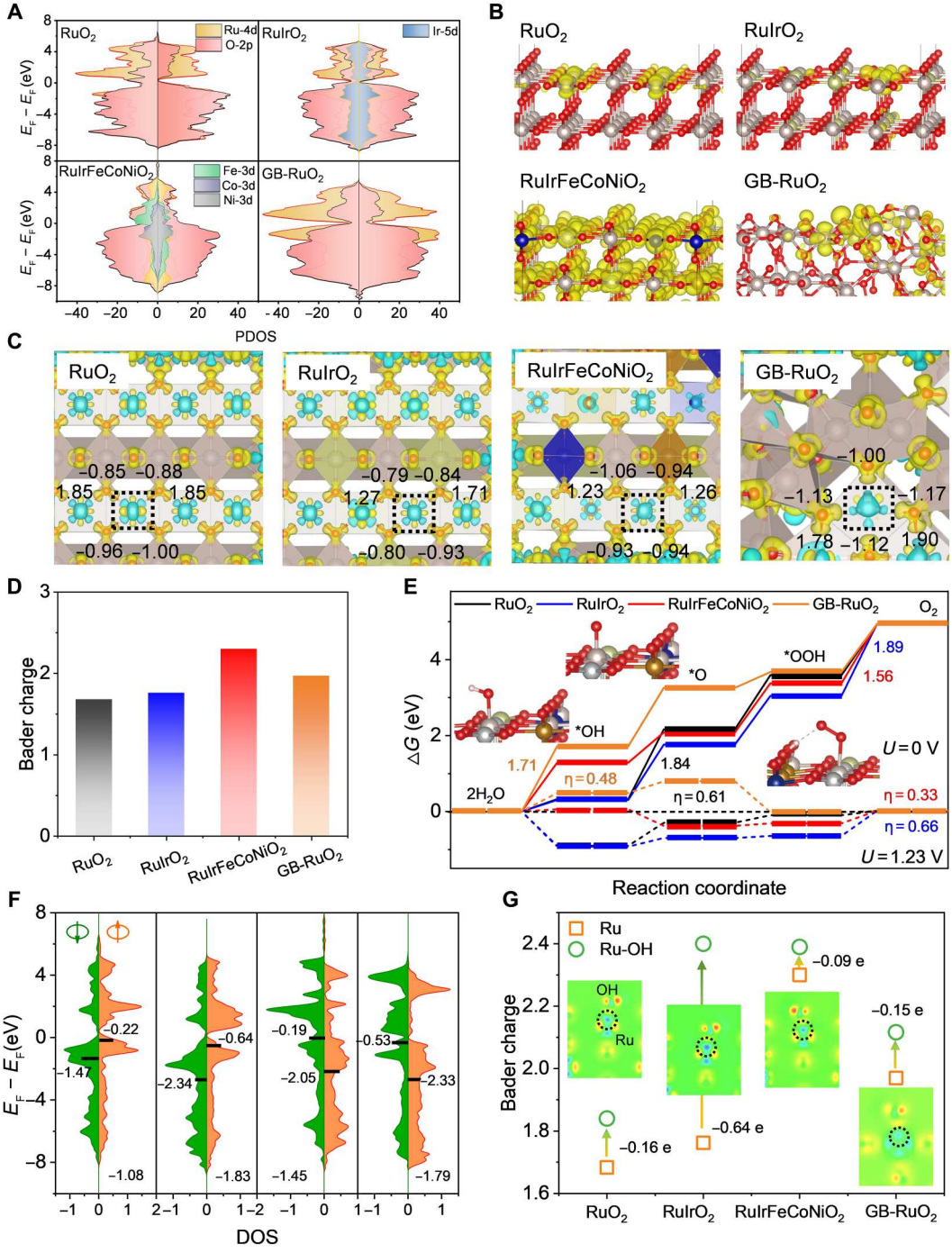

Fig. 5. DFT calculations. (**A**) Partial density of states (PDOS) of RuO_2, $RuIrO_2$, $RuIrFeCoNiO_2$, and GB-RuO_2, respectively. (**B**) Charge density diagram near the fermi energy level from $E_F - 0.1$ to E_F. The isosurface level is set to 0.001 e/A^3. (**C**) Top view of the charge density difference (CDD) of these four models. The RuO_6 octahedron is presented as a polyhedral. The Bader charge of the atoms surrounding the active site is presented in black. (**D**) Bader charge of the active Ru site in different models. (**E**) Free energy diagram for OER over RuO_2, $RuIrO_2$, $RuIrFeCoNiO_2$, and GB-RuO_2 surfaces at zero cell potential ($U = 0$) denoted by a solid line and at the equilibrium potential ($U = 1.23$ V) denoted by a dotted line. (**F**) Projected d DOS of the Ru atom at the active site for different surfaces. The calculated d-band centers for spin-up and spin-down are marked with black lines and the final value is determined by the weighted average denoted at the bottom. (**G**) Bader charge of the Ru at the active site before and after adsorbing OH^-. The insets present the CDD of the OH* model.

activity (*60*). However, there is an important contradiction, not revealed here, where $RuIrO_2$ has the lowest d-band center while exhibiting the strongest adsorption to the intermediates during OER. By following the CDD of the Ru-OH bond in the inset of Fig. 5G (the red area indicates electron accumulation, and the blue area indicates electron depletion), the order of electron loss of Ru atoms on the surface after chemical interaction with OH^- is $RuIrO_2$ > RuO_2 > GB-RuO_2 > $RuIrFeCoNiO_2$. Specifically, the number of transferred electrons of the Ru atom on the $RuIrO_2$ surface is 0.64, much higher than that in the other three models. In the multimetal system, the scaling relationship between O* and OH* is broken. This can be attributed to nonuniform reactions involving adjacent metal atoms and the steric hindrance of lattice O. By combining the changes in Bader charge of the surrounding transition metal and O atoms, we found that in addition to the Ru atom directly involved in adsorption, the nearby atoms on the $RuIrO_2$ surface also undergo severe charge transfer (fig. S48). Although the Ru atoms in $RuIrO_2$ have low activity, as inferred from the d-band center, the strong coupling effect of the surrounding atoms contributes to improving the adsorption activity of OH^-, leading to the low free energy of OH*. In contrast, the OH^- adsorption on the $RuIrFeCoNiO_2$ and GB-RuO_2 surface occurred without marked charge transfer by Ru and surrounding atoms, and the chemical interaction was relatively weak. This behavior effectively coordinates the energy of each elementary step of the OER, thereby reducing the overpotential of the catalytic process. Evidently, the d-band center cannot be used as a single criterion for electrocatalytic activity, and the coordination atoms of the active site should also be considered, at least for the current systems. In summary, the increased OER activity of RuO_2 is attributed to the reduction of $\Delta G(OH^*)$, which can be achieved by co-doping of transition metals and GB formed by different crystallographic orientations of RuO_2, as presented experimentally by the M-$RuIrFeCoNiO_2$.

DISCUSSION

In summary, we present a fast, nonequilibrium route to prepare a sort of multielement, GB-abundant M-$RuIrFeCoNiO_2$ with excellent activity (η_{10} = 189 mV and TOF = 0.24 O_2 s^{-1} at η_{300}) toward acidic OER. It can be even operated at a high current density of 1 A cm^{-2} for over 500 hours in a PEM electrolyzer without obvious performance decay. Ex situ and operando characterizations demonstrate that the intentional introduction of external metal elements and GB would effectively alter the electronic structure and the OER pathway of RuO_2, resulting in enhanced activity and stability. DFT simulations further indicate that the synergistic effects of multiple foreign metal elements and GB can tune the binding energy of oxygen intermediates. Our work proposes a rational design approach of multielement effect and GB enhancement strategy to enhance the acidic OER performance of RuO_2 catalysts.

MATERIALS AND METHODS

Preparation of M-$RuIrFeCoNiO_2$ and M-RuO_2

In a typical procedure for synthesizing M-$RuIrFeCoNiO_2$, 0.5 mmol of $RuCl_3{\cdot}xH_2O$ (Alfa Aesar), 0.25 mmol of $IrCl_3{\cdot}xH_2O$ (Alfa Aesar), 0.25 mmol of $FeCl_3{\cdot}6H_2O$ (Sinopharm Chemical Reagent), 0.25 mmol of $CoCl_2{\cdot}6H_2O$ (Sinopharm Chemical Reagent), and 0.25 mmol of $NiCl_2{\cdot}6H_2O$ (Sinopharm Chemical Reagent) were dissolved in 2 ml of ethanol. After vigorous ultrasound for 1 hour, the homogenous suspension was evaporated in an oven at 60°C. The dried product was ground into fine powder for further use. Subsequently, the crucible containing 0.118 mol of $NaNO_3$ (Sinopharm Chemical Reagent) was heated to 350°C in a muffle furnace with a heating rate of 5°C min^{-1} and maintained at this temperature. After forming a clear liquid, the above-obtained precursor was quickly added into the liquid and annealed at 350°C for 2 hours. The crucible was quickly taken out of the muffle furnace and cooled with water. The product was washed with deionized water and ethanol, then collected by centrifugation, and dried at 80°C overnight. Last, the product with an approximately stoichiometric $(Ru_{0.4}Ir_{0.2}Fe_{0.2}Co_{0.1}Ni_{0.1})O_2$ was obtained and was labeled as $RuIrFeCoNiO_2$ for simplicity. The M-RuO_2 was prepared using the same process except that only the sole Ru source was used during the annealing treatment.

Characterizations

XRD patterns were collected by a SmartLab SE powder diffractometer operating with Cu Kα radiation (λ = 0.15406 nm). TEM was measured on an FEI Tecnai F20 TEM at an accelerating voltage of 300 kV. Scanning electron microscopy EDS was obtained through ZEISS Sigma 300 field emission scanning electron microscope. Annular dark-field scanning transmission electron microscopy images and EELS measurements were obtained from probe Cs-corrected JEM ARM200CF at 200 kV (JEOL Ltd.) and Triple C #3 TEM (an ARM200F-based ultrahigh vacuum microscope equipped with a JEOL delta corrector and a cold field emission gun operating at 60 kV). AFM image was acquired using the Horiba SmartSPM-1000 AFM (Horiba, France). XPS was conducted on an ESCALAB 250 XI x-ray photoelectron spectrometer and Thermo Fisher Scientific K-Alpha (Thermo Fisher Scientific Co., USA) with Al Kα radiation and the C1s peak at 484.8 eV as a calibration standard. N_2 adsorption-desorption measurements were carried out using a Quadrasorb SI Surface Area and Pore Size Analyzer (Quantachrome Ins) at 77 K. The Ru content of the catalysts was measured by ICP-OES (ICAP 7000, Thermo Fisher Scientific Co., USA). ICP-MS was performed on a Thermo Fisher Scientific iCAP RQ ICP-MS system to determine the dissolved metal ions. The produced O_2 was measured by gas chromatography (Agilent, 8890 GC System). The EPR spectra were collected on the Bruker A300.

The operando electrochemical Raman spectroscopy was collected on a confocal microscope Raman system with a 532-nm laser. The electrochemical Raman experiments were performed in a homemade Teflon electrochemical cell. An Autolab PGSTAT30 (Metrohm) potentiostation was used to control the potential during the OER process. Raman frequency was calibrated by a Si wafer (520.6 cm^{-1}) during each experiment.

Ru K-edge of catalysts was collected in transmission mode at the Optique Dispersive EXAFS (ODE) beamline of the Soleil Synchrotron, France. Ir L-edge XAS data were collected in transmission mode at the TPS44A beamline of the National Synchrotron Radiation Research Center (NSRRC), Taiwan. The metal foil of either Ru or Ir was used to calibrate the monochromator energy. O K-edge measurements recorded in the total electron yield mode were performed at the beamline TLS 11A in NSRRC, Taiwan. Processing and fitting of data were processed using the Athena and Artemis programs included in the IFEFFIT software package (*61*, *62*).

Isotope-labeled DEMS measurements were performed on an operando DEMS system, including a mass spectrometer with a high vacuum chamber together with another chamber connecting with the electrochemical cell at ambient pressure. The generated gaseous oxygen products are directly transferred into the vacuum chamber for mass spectrometer analysis. As for the electrochemical system, the Ag/AgCl and Pt wire are served as reference and counter electrodes, respectively. The working electrode is a porous Au film supported on a porous polytetrafluoroethylene membrane. The catalysts ink was dropped cast onto the Au film and naturally dried. First, the catalysts were performed five cycles in ^{18}O-labeled 0.5 M H_2SO_4 electrolyte in the potential range of 1.2 to 1.55 V versus RHE at a scan rate of 5 mV s^{-1} for isotope labeling. Then, ^{18}O-labeled catalysts were rinsed with ^{16}O water to remove the residual $H_2{}^{18}O$. Last, the above catalysts were conducted several cycles in ^{16}O 0.5 M H_2SO_4 electrolyte at the same potential range and scan rate. The gaseous products including $^{32}O_2$, $^{34}O_2$, and $^{36}O_2$ were probed in real time by the mass spectrometer.

Electrochemical OER measurements in a three-electrode system

The electrocatalytic OER properties were evaluated in O_2-saturated 0.5 M H_2SO_4 electrolyte with a three-electrode setup via a CHI 760E electrochemical workstation, using a saturated calomel electrode (SCE) and graphite rod as the reference electrode and the counter electrode, respectively. To better estimate the electrocatalytic performance of the catalysts under a larger current density, the carbon paper (CP) electrode (Shanghai Hesen Electric Co., Ltd.) was used as the working electrode. For the preparation of the catalyst ink, 5 mg of active material with 1 mg of Vulcan XC-72 carbon was homogeneously dispersed into a solution containing 250 μl of ethanol, 250 μl of deionized water, and 25 μl of Nafion (Dupont, 5 wt %). Then, 25 μl of the suspension was drop-casted onto the CP (0.5 cm by 1 cm; catalyst loading: 0.476 mg cm^{-2}) and left to dry naturally at room temperature. For the OER experiment, LSV curves were measured at a scanning rate of 10 mV s^{-1}, and all LSV data presented were iR-compensated (95%). The potential (versus SCE) was converted into RHE values using the following equation: $E_{RHE} = E_{SCE} + 0.2415 + 0.059^*$ pH. The Tafel slope was calculated by the Tafel equation ($\eta = a + b \log j$, where η, a, b, and j represent the overpotential, the intercept, the Tafel slope, and the current density, respectively). EIS (350-mV overpotential) was conducted from 1 Hz to 100 kHz with an amplitude of 10 mV. The electrochemically active surface area (ECSA) for all electrocatalysts was estimated from the electrochemical double-layer capacitance (C_{dl}) at nonfaradaic overpotentials. C_{dl} values were acquired from the linear fitting of double-layer current density versus scan rate. The accelerated stability test of the catalyst was performed through continuous cycling ranging from 1.1 V_{RHE} to 1.5 V_{RHE} for 1000 cycles with a sweep rate of 100 mV s^{-1}.

The MA (j_{MA}) was calculated using the following (Eq. 1) (*63*)

$$j_{MA} = \frac{j_{geo} \times A_{geo}}{m_{noble\ metal}} \quad (1)$$

where j_{geo} is the geometric current density, A_{geo} is the geometric area, and $m_{noble\ metal}$ is the loading mass of noble metal onto the working electrode.

The TOF is generally considered to represent the intrinsic catalytic activity of catalysts. In this work, the TOF values of M-RuIrFeCoNiO_2, M-RuO_2, C-RuO_2, and C-Ir/C were calculated by Eq. 2 (*27*)

$$TOF = \frac{n_{O_2}}{n_{mass}} \quad (2)$$

where n_{O_2} is the number of oxygen molecules and n_{mass} is the number of active sites determined via the total loading mass by assuming noble metal atoms as active sites.

n_{O_2} was calculated by Eq. 3

$$n_{O_2} = \left(j \frac{mA}{cm^2}\right)(A\ cm^2)\left(\frac{1\ \frac{C}{s}}{1000\ mA}\right)\left(\frac{1\ mol\ e^-}{96,485\ C}\right)\left(\frac{1\ mol\ O_2}{4\ mol\ e^-}\right)\left(\frac{6.023 \times 10^{23}\ mol\ O_2}{1\ mol\ O_2}\right) \quad (3)$$

n_{mass} was estimated according to the following (Eq. 4) (*64*)

$$n_{mass} = \frac{m_{loading} \times N_A}{Mw} \times n_{noble\ metal} \quad (4)$$

where $m_{loading}$ is the loading mass of the catalysts, N_A is Avogadro's constant (6.023×10^{23} mol^{-1}), Mw is the molecular weight of catalysts, and $n_{noble\ metal}$ is the number of Ru atoms and/or Ir atoms per molar of the catalysts.

The FE of O_2 generated at different anodic potentials was determined by Eq. 5

$$FE = \frac{4 \times n_{O_2} \times F}{Q} \quad (5)$$

where n_{O_2} (in mole) represents the mole amount of the O_2 gas generated on the results of gas chromatography, F is the Faraday's constant (96,485 C mol^{-1}), and Q (in coulomb) is the total amount of charge passed through the electrochemical cell. It is assumed that the four electrons are needed to produce one O_2 molecule during the OER process.

The S-number was calculated according to the previous literature (*65*) by using the following (Eq. 6)

$$S - number = \frac{n_{O_2}}{n_{noble\ metal}} \quad (6)$$

where n_{O_2} is the molar amount of total oxygen generated during a certain period of time (collected from gas chromatography) and $n_{noble\ metal}$ is the total noble metals (Ru and/or Ir) dissolved in the electrolyte measured by ICP-MS.

Electrochemical OER measurements in a PEM electrolyzer

The membrane electrode assembly (MEA) was constructed to examine the performance of catalysts under actual conditions. Before preparing the MEA, the commercial Nafion 212 membrane (N212, Dupont) was successively pretreated with 5 wt % H_2O_2, 0.5 M H_2SO_4, and deionized water at 80°C for 1 hour, and then preserved in deionized water for further use. The M-RuIrFeCoNiO_2 was used as an anode catalyst, and commercial Pt/C (40 wt %) was used as a cathode catalyst. Appropriate amounts of catalysts were first suspended into a mixture of isopropanol and Nafion ionomer (25 wt % for both anode and cathode) by ultrasonication for 1 hour. Subsequently, the as-prepared ink was sprayed onto the Nafion 212 membrane [catalyst-coated membrane (CCM), surface area: 1.5 cm^2, catalyst mass loading: 2 $mg_{noble\ metal}$ cm^{-2} for anode,

and 0.5 mg_{Pt} cm^{-2} for cathode]. A porous Pt-plated Ti foam and CP served as anodic and cathodic porous gas diffusion layers (GDLs), respectively. Last, the PEM cell was integrated by assembling CCM in the middle of anode and cathode GDLs, equipped with two Ti bipolar plates with the serpentine flow field together. The PEM electrolyzer was maintained at 80°C during the test, using the preheated deionized water as the anode electrolyte (flow rate: 10 ml min^{-1}). The stability performance of catalysts was measured by the chronopotentiometry test at a current density of 1 A cm^{-2}.

Theoretical calculations

All the calculations of geometric and energy are executed within the framework of the DFT method implemented in the Vienna Ab initio Simulation Package (VASP) code (*66*). The exchange-correlation potential was described by the generalized gradient approximation with Perdewe-Burkee-Ernzerhof functional (*67*). The projector-augmented wave method was used to account for core-valence interactions (*68*, *69*). The kinetic energy cutoff for plane wave expansions was set to 600 eV, and reciprocal space was sampled by the gamma-centered k-mesh with a resolution of 0.03 in the unit of 2*PI/Å, depending on the model. The vacuum layer is at least 15 Å in the *z* direction to minimize possible interactions between the replicated cells. The convergence criteria are 1×10^{-5} eV energy differences for solving the electronic wave function, and the structures were relaxed until the forces on all atoms were smaller than −0.02 eV/Å. A post-stage Van der Waals DFT-D3 method with Becke-Johnson damping was applied (*70*) and the Hubbard *U* corrections to the d electrons of Ru and Ir following the approach proposed by Dudarev *et al.* (*71*) were considered. The values of the effective Hubbard *U* parameter, *U* = 3.8 eV and 4.2 eV, are chosen for Ru and Ir, respectively, determined by the linear response approach (*72*). The climbing image nudged elastic band method (*73*) as implemented in VASP was used to locate the transition state.

The free energy Δ*G* for each OER step was calculated through the model of computational hydrogen electrode along with the equation as follows (Eq. 7)

$$\Delta G = \Delta E_{\mathrm{DFT}} + \Delta \mathrm{ZPE} - T\Delta S \quad (7)$$

where ΔE_{DFT}, ΔZPE, Δ*S*, and *T* are the changes in DFT energy, zero-point energy, entropy from the initial state to the final state, and temperature, respectively. ΔZPE and Δ*S* can be obtained from the NIST-JANAF thermodynamics table (*74*) for gaseous molecules and by calculating the vibrational frequencies for the reactive intermediates, respectively. The energies of H_2O and H_2 molecules calculated by DFT together with the experimental formation energy of H_2O (4.92 eV) were used to establish the free energy diagram. The free energies of OOH*, O*, OH*, and O_2, at a given potential *U*, were calculated relative to RHE.

For pure RuO_2, a 4 × 3 × 4 RuO_2(110) surface slab model was constructed, with the bottom two layers fixed to mimic the bulk structure. $(Ru_{0.7}Ir_{0.3})O_2$ and $(Ru_{0.4}Ir_{0.2}Fe_{0.2}Co_{0.1}Ni_{0.1})O_2$ models were constructed by replacing the Ru atoms with the transition metal atoms using a normal distribution algorithm. The interface was constructed by the RuO_2(111) with different crystallographic according to experimental observation.

The formation energy of O vacancy (E_O) is defined as (Eq. 8)

$$E_O = E_{\mathrm{def}}(O) - E_{\mathrm{total}} + \mu_O \quad (8)$$

where E_{total} is the energy of the slab. E_{def}(O) and μ_O are the energy of the slab when one O atom is removed and the chemical potential of the O which is referenced to O_2 gas at 0 K, respectively. The energy required for the demetallization of metal (E_{de}) is calculated by Eq. 9

$$E_{\mathrm{de}} = E_{\mathrm{def}}(m) - E_{\mathrm{total}} + \mu_m \quad (9)$$

where $E_{\mathrm{def}}(m)$ and μ_m are the energy of the slab when one metal atom is removed and the chemical potential of the metal atom which is referenced to its most stable simple substance, respectively.

The special quasi-random structure method (*75*), which is coded as "mcsqs" (*76*) in the Alloy Theoretical Automated Toolkit, was used to construct the structural models for high-entropy oxides.

Supplementary Materials

This PDF file includes:

Figs. S1 to S48
Tables S1 to S7
Supplementary Note
References

REFERENCES AND NOTES

1. H. Dotan, A. Landman, S. W. Sheehan, K. D. Malviya, G. E. Shter, D. A. Grave, Z. Arzi, N. Yehudai, M. Halabi, N. Gal, N. Hadari, C. Cohen, A. Rothschild, G. S. Grader, Decoupled hydrogen and oxygen evolution by a two-step electrochemical–chemical cycle for efficient overall water splitting. *Nat. Energy* **4**, 786–795 (2019).
2. V. R. Stamenkovic, D. Strmcnik, P. P. Lopes, N. M. Markovic, Energy and fuels from electrochemical interfaces. *Nat. Mater.* **16**, 57–69 (2016).
3. J. Kibsgaard, I. Chorkendorff, Considerations for the scaling-up of water splitting catalysts. *Nat. Energy* **4**, 430–433 (2019).
4. H. Zhang, S. Zuo, M. Qiu, S. Wang, Y. Zhang, J. Zhang, X. W. D. Lou, Direct probing of atomically dispersed Ru species over multi-edged TiO_2 for highly efficient photocatalytic hydrogen evolution. *Sci. Adv.* **6**, eabb9823 (2020).
5. M. Carmo, D. L. Fritz, J. Mergel, D. Stolten, A comprehensive review on PEM water electrolysis. *Int. J. Hydrogen Energy* **38**, 4901–4934 (2013).
6. M. Lu, Y. Zheng, Y. Hu, B. Huang, D. Ji, M. Sun, J. Li, Y. Peng, R. Si, P. Xi, C.-H. Yan, Artificially steering electrocatalytic oxygen evolution reaction mechanism by regulating oxygen defect contents in perovskites. *Sci. Adv.* **8**, eabq3563 (2022).
7. X. Wu, H. Zhang, S. Zuo, J. Dong, Y. Li, J. Zhang, Y. Han, Engineering the coordination sphere of isolated active sites to explore the intrinsic activity in single-atom catalysts. *Nanomicro Lett.* **13**, 136 (2021).
8. M. Bernt, A. Hartig-Weiß, M. F. Tovini, H. A. El-Sayed, C. Schramm, J. Schröter, C. Gebauer, H. A. Gasteiger, Current challenges in catalyst development for PEM water electrolyzers. *Chem. Ing. Tech. (Weinh)* **92**, 31–39 (2020).
9. H. Zhang, W. Zhou, X. F. Lu, T. Chen, X. W. Lou, Implanting isolated Ru atoms into edge-rich carbon matrix for efficient electrocatalytic hydrogen evolution. *Adv. Energy Mater.* **10**, 2000882 (2020).
10. S. Zuo, Z.-P. Wu, H. Zhang, X. W. Lou, Operando monitoring and deciphering the structural evolution in oxygen evolution electrocatalysis. *Adv. Energy Mater.* **12**, 2103383 (2022).
11. R. R. Rao, M. J. Kolb, L. Giordano, A. F. Pedersen, Y. Katayama, J. Hwang, A. Mehta, H. You, J. R. Lunger, H. Zhou, N. B. Halck, T. Vegge, I. Chorkendorff, I. E. L. Stephens, Y. Shao-Horn, Operando identification of site-dependent water oxidation activity on ruthenium dioxide single-crystal surfaces. *Nat. Catal.* **3**, 516–525 (2020).
12. K. A. Stoerzinger, R. R. Rao, X. R. Wang, W. T. Hong, C. M. Rouleau, Y. Shao-Horn, The role of Ru redox in pH-dependent oxygen evolution on rutile ruthenium dioxide surfaces. *Chem* **2**, 668–675 (2017).
13. R. Kötz, S. Stucki, D. Scherson, D. M. Kolb, In-situ identification of RuO_4 as the corrosion product during oxygen evolution on ruthenium in acid media. *J. Electroanal. Chem.* **172**, 211–219 (1984).
14. J. Shan, C. Guo, Y. Zhu, S. Chen, L. Song, M. Jaroniec, Y. Zheng, S.-Z. Qiao, Charge-redistribution-enhanced nanocrystalline Ru@IrO_x electrocatalysts for oxygen evolution in acidic media. *Chem* **5**, 445–459 (2019).
15. J. Wang, L. Han, B. Huang, Q. Shao, H. L. Xin, X. Huang, Amorphization activated ruthenium-tellurium nanorods for efficient water splitting. *Nat. Commun.* **10**, 5692 (2019).

16. X. Cui, P. Ren, C. Ma, J. Zhao, R. Chen, S. Chen, N. P. Rajan, H. Li, L. Yu, Z. Tian, D. Deng, Robust interface Ru centers for high-performance acidic oxygen evolution. *Adv. Mater.* **32**, e1908126 (2020).
17. A. M. Harzandi, S. Shadman, A. S. Nissimagoudar, D. Y. Kim, H. D. Lim, J. H. Lee, M. G. Kim, H. Y. Jeong, Y. Kim, K. S. Kim, Ruthenium core–shell engineering with nickel single atoms for selective oxygen evolution via nondestructive mechanism. *Adv. Energy Mater.* **11**, 2003448 (2021).
18. J. Shan, T. Ling, K. Davey, Y. Zheng, S.-Z. Qiao, Transition-metal-doped RuIr bifunctional nanocrystals for overall water splitting in acidic environments. *Adv. Mater.* **31**, e1900510 (2019).
19. M. Retuerto, L. Pascual, F. Calle-Vallejo, P. Ferrer, D. Gianolio, A. G. Pereira, A. Garcia, J. Torrero, M. T. Fernandez-Diaz, P. Bencok, M. A. Pena, J. L. G. Fierro, S. Rojas, Na-doped ruthenium perovskite electrocatalysts with improved oxygen evolution activity and durability in acidic media. *Nat. Commun.* **10**, 2041 (2019).
20. Y. Lin, Z. Tian, L. Zhang, J. Ma, Z. Jiang, B. J. Deibert, R. Ge, L. Chen, Chromium-ruthenium oxide solid solution electrocatalyst for highly efficient oxygen evolution reaction in acidic media. *Nat. Commun.* **10**, 162 (2019).
21. V. R. Stamenkovic, B. S. Mun, M. Arenz, K. J. Mayrhofer, C. A. Lucas, G. Wang, P. N. Ross, N. M. Markovic, Trends in electrocatalysis on extended and nanoscale Pt-bimetallic alloy surfaces. *Nat. Mater.* **6**, 241–247 (2007).
22. T. Reier, Z. Pawolek, S. Cherevko, M. Bruns, T. Jones, D. Teschner, S. Selve, A. Bergmann, H. N. Nong, R. Schlogl, K. J. J. Mayrhofer, P. Strasser, Molecular insight in structure and activity of highly efficient, low-Ir Ir-Ni oxide catalysts for electrochemical water splitting (OER). *J. Am. Chem. Soc.* **137**, 13031–13040 (2015).
23. M. Luo, S. Guo, Strain-controlled electrocatalysis on multimetallic nanomaterials. *Nat. Rev. Mater.* **2**, 17059 (2017).
24. H. Flood, T. Forland, The acidic and basic properties of oxides. *Acta Chem. Scand.* **1**, 592–604 (1947).
25. D. H. Kerridge, W. M. Shakir, Molten lithium nitrate-potassium nitrate eutectic: The reaction of tin(II) chloride. *Thermochim. Acta* **136**, 149–152 (1988).
26. E. D. Bøjesen, B. B. Iversen, The chemistry of nucleation. *CrystEngComm* **18**, 8332–8353 (2016).
27. S. Hao, H. Sheng, M. Liu, J. Huang, G. Zheng, F. Zhang, X. Liu, Z. Su, J. Hu, Y. Qian, L. Zhou, Y. He, B. Song, L. Lei, X. Zhang, S. Jin, Torsion strained iridium oxide for efficient acidic water oxidation in proton exchange membrane electrolyzers. *Nat. Nanotechnol.* **16**, 1371–1377 (2021).
28. R. L. Penn, J. F. Banfield, Imperfect oriented attachment: Dislocation generation in defect-free nanocrystals. *Science* **281**, 969–971 (1998).
29. J. J. De Yoreo, P. U. P. A. Gilbert, N. A. J. M. Sommerdijk, R. L. Penn, S. Whitelam, D. Joester, H. Zhang, J. D. Rimer, A. Navrotsky, J. F. Banfield, A. F. Wallace, F. M. Michel, F. C. Meldrum, H. Colfen, P. M. Dove, Crystallization by particle attachment in synthetic, biogenic, and geologic environments. *Science* **349**, 6247 (2015).
30. J. Y. Shen, A. Adnot, S. Kaliaguine, An ESCA study of the interaction of oxygen with the surface of ruthenium. *Appl. Surf. Sci.* **51**, 47–60 (1991).
31. M. C. Biesinger, B. P. Payne, A. P. Grosvenor, L. W. M. Lau, A. R. Gerson, R. S. C. Smart, Resolving surface chemical states in XPS analysis of first row transition metals, oxides and hydroxides: Cr, Mn, Fe, Co and Ni. *Appl. Surf. Sci.* **257**, 2717–2730 (2011).
32. S. Hao, M. Liu, J. Pan, X. Liu, X. Tan, N. Xu, Y. He, L. Lei, X. Zhang, Dopants fixation of ruthenium for boosting acidic oxygen evolution stability and activity. *Nat. Commun.* **11**, 5368 (2020).
33. D. A. McKeown, P. L. Hagans, L. P. L. Carette, A. E. Russell, K. E. Swider, D. R. Rolison, Structure of hydrous ruthenium oxides: Implications for charge storage. *J. Phys. Chem. B* **103**, 4825–4832 (1999).
34. Y. Mo, I. T. Bae, S. Sarangapani, D. A. Scherson, In situ Ru K-edge X-ray absorption spectroscopy of a high-area ruthenium dioxide electrode in a Nafion-based supercapacitor environment. *J. Solid State Electr.* **7**, 572–575 (2003).
35. L. Zhuang, L. Ge, Y. Yang, M. Li, Y. Jia, X. Yao, Z. Zhu, Ultrathin iron-cobalt oxide nanosheets with abundant oxygen vacancies for the oxygen evolution reaction. *Adv. Mater.* **29**, 1606793 (2017).
36. Q. Yang, Y. Jia, F. Wei, L. Zhuang, D. Yang, J. Liu, X. Wang, S. Lin, P. Yuan, X. Yao, Understanding the activity of Co-$N_{4-x}C_x$ in atomic metal catalysts for oxygen reduction catalysis. *Angew. Chem. Int. Ed. Engl.* **59**, 6122–6127 (2020).
37. H. M. Tsai, P. D. Babu, C. W. Pao, J. W. Chiou, J. C. Jan, K. P. Krishna Kumar, F. Z. Chien, W. F. Pong, M.-H. Tsai, C.-H. Chen, L. Y. Jang, J. F. Lee, R. S. Chen, Y. S. Huang, D. S. Tsai, Comparison of electronic structures of RuO_2 and IrO_2 nanorods investigated by x-ray absorption and scanning photoelectron microscopy. *Appl. Phys. Lett.* **90**, 042108 (2007).
38. Z. Y. Wu, S. Gota, F. Jollet, M. Pollak, M. Gautier-Soyer, C. R. Natoli, Characterization of iron oxides by x-ray absorption at the oxygen K edgeusing a full multiple-scattering approach. *Phys. Rev. B* **55**, 2570–2577 (1997).
39. A. K. Sinha, M. N. Singh, S. N. Achary, A. Sagdeo, D. K. Shukla, D. M. Phase, Crystal field splitting and spin states of Co ions in cobalt ferrite with composition $Co_{1.5}Fe_{1.5}O_4$ using magnetization and X-ray absorption spectroscopy measurements. *J. Magn. Magn. Mater.* **435**, 87–95 (2017).
40. Z. Y. Wu, C. M. Liu, L. Guo, R. Hu, M. I. Abbas, T. D. Hu, H. B. Xu, Structural characterization of nickel oxide nanowires by X-ray absorption near-edge structure spectroscopy. *J. Phys. Chem. B* **109**, 2512–2515 (2005).
41. Z. Y. Wu, F. Y. Chen, B. Li, S. W. Yu, Y. Z. Finfrock, D. M. Meira, Q. Q. Yan, P. Zhu, M. X. Chen, T. W. Song, Z. Yin, H. W. Liang, S. Zhang, G. Wang, H. Wang, Non-iridium-based electrocatalyst for durable acidic oxygen evolution reaction in proton exchange membrane water electrolysis. *Nat. Mater.* **22**, 100–108 (2023).
42. H. H. Pham, M.-J. Cheng, H. Frei, L.-W. Wang, Surface proton hopping and fast-kinetics pathway of water oxidation on Co_3O_4 (001) surface. *ACS Catal.* **6**, 5610–5617 (2016).
43. S. Y. Mar, C. S. Chen, Y. S. Huang, K. K. Tiong, Characterization of RuO_2 thin films by Raman spectroscopy. *Appl. Surf. Sci.* **90**, 497–504 (1995).
44. Y. Lee, H.-Y. Shin, S. H. Chun, J. Lee, W. J. Park, J. M. Baik, S. Yoon, M. H. Kim, Highly single crystalline $Ir_xRu_{1-x}O_2$ mixed metal oxide nanowires. *J. Phys. Chem. C* **116**, 16300–16304 (2012).
45. Y. S. Huang, F. H. Pollak, Raman investigation of rutile RuO_2. *Solid State Commun.* **43**, 921–924 (1982).
46. H. C. Jo, K. M. Kim, H. Cheong, S.-H. Lee, S. K. Deb, In situ Raman spectroscopy of $RuO_2 \cdot xH_2O$. *Electrochem. Solid St.* **8**, E39–E41 (2005).
47. Z. Pavlovic, C. Ranjan, Q. Gao, M. van Gastel, R. Schlögl, Probing the structure of a water-oxidizing anodic iridium oxide catalyst using Raman spectroscopy. *ACS Catal.* **6**, 8098–8105 (2016).
48. N. Hodnik, P. Jovanovič, A. Pavlišič, B. Jozinović, M. Zorko, M. Bele, V. S. Šelih, M. Šala, S. Hočevar, M. Gaberšček, New insights into corrosion of ruthenium and ruthenium oxide nanoparticles in acidic media. *J. Phys. Chem. C* **119**, 10140–10147 (2015).
49. J. Qi, M. Yang, H. Zeng, Y. Jiang, L. Gu, W. Zhao, Z. Liu, T. Liu, C. Yang, R. Si, Understanding the stabilization effect of the hydrous IrO_x layer formed on the iridium oxide surface during the oxygen evolution reaction in acid. *Inorg. Chem. Front.* **10**, 776–786 (2023).
50. C. Roy, R. R. Rao, K. A. Stoerzinger, J. Hwang, J. Rossmeisl, I. Chorkendorff, Y. Shao-Horn, I. E. L. Stephens, Trends in activity and dissolution on RuO_2 under oxygen evolution conditions: Particles versus well-defined extended surfaces. *ACS Energy Lett.* **3**, 2045–2051 (2018).
51. O. Kasian, S. Geiger, T. Li, J.-P. Grote, K. Schweinar, S. Zhang, C. Scheu, D. Raabe, S. Cherevko, B. Gault, K. J. J. Mayrhofer, Degradation of iridium oxides via oxygen evolution from the lattice: Correlating atomic scale structure with reaction mechanisms. *Energy Environ. Sci.* **12**, 3548–3555 (2019).
52. S. B. Scott, J. E. Sorensen, R. R. Rao, C. Moon, J. Kibsgaard, Y. Shao-Horn, I. Chorkendorff, The low overpotential regime of acidic water oxidation part II: Trends in metal and oxygen stability numbers. *Energ. Environ. Sci.* **15**, 1988–2001 (2022).
53. H. B. Tao, Y. Xu, X. Huang, J. Chen, L. Pei, J. Zhang, J. G. Chen, B. Liu, A general method to probe oxygen evolution intermediates at operating conditions. *Joule* **3**, 1498–1509 (2019).
54. J. S. de Almeida, R. Ahuja, Electronic and optical properties of RuO_2 and IrO_2. *Phys. Rev. B* **73**, 165102 (2006).
55. N. Mehtougui, D. Rached, R. Khenata, H. Rached, M. Rabah, S. Bin-Omran, Structural, electronic and mechanical properties of RuO_2 from first-principles calculations. *Mater. Sci. Semicond. Process.* **15**, 331–339 (2012).
56. L. Zhang, H. Jang, H. Liu, M. G. Kim, D. Yang, S. Liu, X. Liu, J. Cho, Sodium-decorated amorphous/crystalline RuO_2 with rich oxygen vacancies: A robust pH-universal oxygen evolution electrocatalyst. *Angew. Chem. Int. Ed.* **60**, 18821–18829 (2021).
57. J. K. Norskov, J. Rossmeisl, A. Logadottir, L. Lindqvist, J. R. Kitchin, T. Bligaard, H. Jonsson, Origin of the overpotential for oxygen reduction at a fuel-cell cathode. *J. Phys. Chem. B* **108**, 17886–17892 (2004).
58. R. R. Rao, M. J. Kolb, N. B. Halck, A. F. Pedersen, A. Mehta, H. You, K. A. Stoerzinger, Z. Feng, H. A. Hansen, H. Zhou, L. Giordano, J. Rossmeisl, T. Vegge, I. Chorkendorff, I. E. L. Stephens, Y. Shao-Horn, Towards identifying the active sites on RuO_2(110) in catalyzing oxygen evolution. *Energy Environ. Sci.* **10**, 2626–2637 (2017).
59. L. Yang, G. Yu, X. Ai, W. Yan, H. Duan, W. Chen, X. Li, T. Wang, C. Zhang, X. Huang, J. S. Chen, X. Zou, Efficient oxygen evolution electrocatalysis in acid by a perovskite with face-sharing IrO_6 octahedral dimers. *Nat. Commun.* **9**, 5236 (2018).
60. B. Hammer, J. K. Nørskov, Electronic factors determining the reactivity of metal surfaces. *Surf. Sci.* **343**, 211–220 (1995).
61. B. Ravel, M. Newville, ATHENA, ARTEMIS, HEPHAESTUS: Data analysis for X-ray absorption spectroscopy using IFEFFIT. *J. Synchrotron Radiat.* **12**, 537–541 (2005).
62. M. Newville, IFEFFIT: Interactive XAFS analysis and FEFF fitting. *J. Synchrotron Radiat.* **8**, 322–324 (2001).

63. C. Lin, J.-L. Li, X. Li, S. Yang, W. Luo, Y. Zhang, S.-H. Kim, D.-H. Kim, S. S. Shinde, Y.-F. Li, Z.-P. Liu, Z. Jiang, J.-H. Lee, In-situ reconstructed Ru atom array on α-MnO_2 with enhanced performance for acidic water oxidation. *Nat. Catal.* **4**, 1012–1023 (2021).
64. Y. Wen, P. Chen, L. Wang, S. Li, Z. Wang, J. Abed, X. Mao, Y. Min, C. T. Dinh, P. Luna, R. Huang, L. Zhang, L. Wang, L. Wang, R. J. Nielsen, H. Li, T. Zhuang, C. Ke, O. Voznyy, Y. Hu, Y. Li, W. A. Goddard III, B. Zhang, H. Peng, E. H. Sargent, Stabilizing highly active Ru sites by suppressing lattice oxygen participation in acidic water oxidation. *J. Am. Chem. Soc.* **143**, 6482–6490 (2021).
65. S. Geiger, O. Kasian, M. Ledendecker, E. Pizzutilo, A. M. Mingers, W. T. Fu, O. Diaz-Morales, Z. Li, T. Oellers, L. Fruchter, A. Ludwig, K. J. J. Mayrhofer, M. T. M. Koper, S. Cherevko, The stability number as a metric for electrocatalyst stability benchmarking. *Nat. Catal.* **1**, 508–515 (2018).
66. J. Hafner, Materials simulations using VASP—A quantum perspective to materials science. *Comput. Phys. Commun.* **177**, 6–13 (2007).
67. G. Kresse, J. Furthmuller, Efficient iterative schemes for ab initio total-energy calculations using a plane-wave basis set. *Phys. Rev. B Condens. Matter* **54**, 11169–11186 (1996).
68. J. P. Perdew, J. A. Chevary, S. H. Vosko, K. A. Jackson, M. R. Pederson, D. J. Singh, C. Fiolhais, Atoms, molecules, solids, and surfaces: Applications of the generalized gradient approximation for exchange and correlation. *Phys. Rev. B Condens. Matter.* **46**, 6671–6687 (1992).
69. J. P. Perdew, J. A. Chevary, S. H. Vosko, K. A. Jackson, M. R. Pederson, D. J. Singh, C. Fiolhais, Erratum: Atoms, molecules, solids, and surfaces: Applications of the generalized gradient approximation for exchange and correlation. *Phys. Rev. B Condens. Matter.* **48**, 4978 (1993).
70. S. Grimme, S. Ehrlich, L. Goerigk, Effect of the damping function in dispersion corrected density functional theory. *J. Comput. Chem.* **32**, 1456–1465 (2011).
71. S. L. Dudarev, G. A. Botton, S. Y. Savrasov, C. J. Humphreys, A. P. Sutton, Electron-energy-loss spectra and the structural stability of nickel oxide: An LSDA + U study. *Phys. Rev. B* **57**, 1505–1509 (1998).
72. M. Cococcioni, S. de Gironcoli, Linear response approach to the calculation of the effective interaction parameters in the LDA+U method. *Phys. Rev. B* **71**, 035105 (2005).
73. G. Henkelman, B. P. Uberuaga, H. Jonsson, A climbing image nudged elastic band method for finding saddle points and minimum energy paths. *J. Chem. Phys.* **113**, 9901–9904 (2000).
74. American Institute of Physics, *FYI: Science Policy News* (1998); www.aip.org/fyi/yearly-archive/1998.
75. A. Zunger, S.-H. Wei, L. G. Ferreira, J. E. Bernard, Special quasirandom structures. *Phys. Rev. Lett.* **65**, 353–356 (1990).
76. A. van de Walle, P. Tiwary, M. de Jong, D. L. Olmsted, M. Asta, A. Dick, D. Shin, Y. Wang, L.-Q. Chen, Z.-K. Liu, Efficient stochastic generation of special quasirandom structures. *CALPHAD* **42**, 13–18 (2013).
77. L. Zhuang, F. Xu, K. Wang, J. Li, C. Liang, W. Zhou, Z. Xu, Z. Shao, Z. Zhu, Porous structure engineering of iridium oxide nanoclusters on atomic scale for efficient pH-universal overall water splitting. *Small* **17**, e2100121 (2021).
78. Q. Dang, H. Lin, Z. Fan, L. Ma, Q. Shao, Y. Ji, F. Zheng, S. Geng, S. Z. Yang, N. Kong, W. Zhu, Y. Li, F. Liao, X. Huang, M. Shao, Iridium metallene oxide for acidic oxygen evolution catalysis. *Nat. Commun.* **12**, 6007 (2021).
79. Q. Yao, B. Huang, Y. Xu, L. Li, Q. Shao, X. Huang, A chemical etching strategy to improve and stabilize RuO_2-based nanoassemblies for acidic oxygen evolution. *Nano Energy* **84**, 105909 (2021).
80. N. Li, L. Cai, C. Wang, Y. Lin, J. Huang, H. Sheng, H. Pan, W. Zhang, Q. Ji, H. Duan, W. Hu, W. Zhang, F. Hu, H. Tan, Z. Sun, B. Song, S. Jin, W. Yan, Identification of the active-layer structures for acidic oxygen evolution from 9R-$BaIrO_3$ electrocatalyst with enhanced iridium mass activity. *J. Am. Chem. Soc.* **143**, 18001–18009 (2021).
81. Y. Xue, J. Fang, X. Wang, Z. Xu, Y. Zhang, Q. Lv, M. Liu, W. Zhu, Z. Zhuang, Sulfate-functionalized RuFeOx as highly efficient oxygen evolution reaction electrocatalyst in acid. *Adv. Funct. Mater.* **31**, 2101405 (2021).
82. J. He, X. Zhou, P. Xu, J. Sun, Regulating electron redistribution of intermetallic iridium oxide by incorporating Ru for efficient acidic water oxidation. *Adv. Energy Mater.* **11**, 2102883 (2021).
83. Q. Qin, H. Jang, Y. Wang, L. Zhang, Z. Li, M. G. Kim, S. Liu, X. Liu, J. Cho, Gettering La effect from La_3IrO_7 as a highly efficient electrocatalyst for oxygen evolution reaction in acid media. *Adv. Energy Mater.* **11**, 2003561 (2020).
84. Z. L. Zhao, Q. Wang, X. Huang, Q. Feng, S. Gu, Z. Zhang, H. Xu, L. Zeng, M. Gu, H. Li, Boosting the oxygen evolution reaction using defect-rich ultra-thin ruthenium oxide nanosheets in acidic media. *Energy Environ. Sci.* **13**, 5143–5151 (2020).
85. D. Chen, T. Liu, P. Wang, J. Zhao, C. Zhang, R. Cheng, W. Li, P. Ji, Z. Pu, S. Mu, Ionothermal route to phase-pure RuB_2 Catalysts for efficient oxygen evolution and water splitting in acidic media. *ACS Energy Lett.* **5**, 2909–2915 (2020).
86. J. Xu, Z. Lian, B. Wei, Y. Li, O. Bondarchuk, N. Zhang, Z. Yu, A. Araujo, I. Amorim, Z. Wang, B. Li, L. Liu, Strong electronic coupling between ultrafine iridium–ruthenium nanoclusters and conductive, acid-stable tellurium nanoparticle support for efficient and durable oxygen evolution in acidic and neutral Media. *ACS Catal.* **10**, 3571–3579 (2020).
87. L. Cao, Q. Luo, J. Chen, L. Wang, Y. Lin, H. Wang, X. Liu, X. Shen, W. Zhang, W. Liu, Z. Qi, Z. Jiang, J. Yang, T. Yao, Dynamic oxygen adsorption on single-atomic ruthenium catalyst with high performance for acidic oxygen evolution reaction. *Nat. Commun.* **10**, 4849 (2019).
88. Y. Yao, S. Hu, W. Chen, Z.-Q. Huang, W. Wei, T. Yao, R. Liu, K. Zang, X. Wang, G. Wu, W. Yuan, T. Yuan, B. Zhu, W. Liu, Z. Li, D. He, Z. Xue, Y. Wang, X. Zheng, J. Dong, C.-R. Chang, Y. Chen, X. Hong, J. Luo, S. Wei, W.-X. Li, P. Strasser, Y. Wu, Y. Li, Engineering the electronic structure of single atom Ru sites via compressive strain boosts acidic water oxidation electrocatalysis. *Nat. Catal.* **2**, 304–313 (2019).
89. R. Ge, L. Li, J. Su, Y. Lin, Z. Tian, L. Chen, Ultrafine defective RuO_2 electrocatayst integrated on carbon cloth for robust water oxidation in acidic media. *Adv. Energy Mater.* **9**, 1901313 (2019).
90. S. Laha, Y. Lee, F. Podjaski, D. Weber, V. Duppel, L. M. Schoop, F. Pielnhofer, C. Scheurer, K. Müller, U. Starke, K. Reuter, B. V. Lotsch, Ruthenium oxide nanosheets for enhanced oxygen evolution catalysis in acidic medium. *Adv. Energy Mater.* **9**, 1803795 (2019).
91. K. Chen, J. Ma, H. Wang, C. Li, L. An, Entropy-stabilized oxides with medium configurational entropy. *Ceram. Int.* **47**, 9979–9983 (2021).

Acknowledgments

Funding: This work was financially supported by the National Key R&D Program of China (2020YFB1505802), the Ministry of Science and Technology (2017YFA0208200), the National Natural Science Foundation of China (22025108, U21A20327, 22121001, and 52122211), the Postdoctoral Science Foundation of China (2021 M702731), the JSPS KAKENHI (22F22358), and the start-up fundings from Xiamen University. **Author contributions:** X.H. supervised the project. C.H. carried out the materials design, electrochemical experiments, data processing and analysis, the fabrication of membrane electrode assembly, and manuscript writing. K.Y. and X.W. conducted the PEM measurements. J.H. performed the DFT calculations. X.L., D.S., Q.L., and K.S. performed part of electron microscopy experiments. Q.K., C.-W.P., and Z.H. performed the XAS measurements. L.L. analyzed the XAS data. Y.T. and Q.Z. contacted the cooperation. All authors wrote and commented on the manuscript. **Competing interests:** The authors declare that they have no competing interests. **Data and materials availability:** All data needed to evaluate the conclusions in the paper are present in the paper and/or the Supplementary Materials.

Submitted 20 November 2022
Accepted 14 August 2023
Published 15 September 2023
10.1126/sciadv.adf9144